Numerical simulation of reactive species transfer at a spherical gas bubble

Numerische Simulation des reaktiven Stoffübergangs an einer sphärischen Gasblase
Bachelor-Thesis of Tim Jeremy Patrick Karpowski from Darmstadt
Date of submission: 20.09.17

1. Supervisor: Prof. Dr. Dieter Bothe
2. Supervisor: Prof. Dr. Peter Stephan

TECHNISCHE
UNIVERSITÄT
DARMSTADT

Mathematical Modeling and Analysis
Center of Smart Interfaces

Numerical simulation of reactive species transfer at a spherical gas bubble
Numerische Simulation des reaktiven Stoffübergangs an einer sphärischen Gasblase

Submitted Bachelor-Thesis of Tim Jeremy Patrick Karpowski born in Darmstadt

1. Supervisor: Prof. Dr. Dieter Bothe
2. Supervisor: Prof. Dr. Peter Stephan

Date of submission: 20.09.17

Abstract

The reactive mass transfer at spherical gas bubbles in a stationary incompressible fluid is analysed numerically. Only the continuous phase is simulated. The influence of the gaseous phase on mass transfer is neglected. The concentration of the transfer species, which diffuses into the bulk, is assumed to be constant in space and time inside the bubble. Four different reaction types, namely decay , single, parallel consecutive and parallel competitive reaction are evaluated all being irreversible and of first order for the transfer species A. The main parameters for mass transfer are accessed and a parameter study is carried out to quantify their influence. The parameters studied are $Re \in [2; 100]$, $Pe \in [10^4; 10^6]$, $Da \in [0, 10]$ and different ratios of concentrations c_i/c_A and diffusivities D_i/D_A, both in the range of $[0.1; 10]$.The data is then compared with known correlations for non-reactive mass transfer and the enhancement factor. Afterwards regression algorithms from the field of machine learning are implemented and trained on the data sets. The performance of the algorithms is accessed. A trained algorithm is used to predict the mass transfer and the resulting volume change at a rising CO_2 bubble in Water. The effect of conjugated mass transfer is analysed and the results are compared to experimental data.

Der reaktive Stofftransfer an sphärischen Gasblasen in einem stationären inkompressiblen Fluid wird numerisch analysiert. Nur die kontinuierliche Phase wird simuliert. Der Einfluss der Gasphase auf den Stoffaustausch wird vernachlässigt. Es wird angenommen, dass die Konzentration der Transferspezies, welche in die Bulk Phase diffundiert, inerhalb der Blase zeitlich und räumlich konstant ist. Es werden vier verschiedene Reaktionstypen, namentlich decay, single, parallel consecutive und parallel competitive Reaktion ausgewertet. Alle Reaktionen sind irreversibel und erster Ordnung für die Transferspezies A. Die Hauptparameter für den Stoffübergang werden bestimmt und eine Parameterstudie wird durchgeführt, um ihren Einfluss zu quantifizieren. Untersucht werden $Re \in [2; 100]$, $Pe \in [10^4; 10^6]$, $Da \in [0, 10]$ und unterschiedliche Konzentrations c_i/c_A und Diffusivitätsverhältnisse D_i/D_A, beide im Bereich von $[0.1; 10]$. Die Daten werden anschließend mit bekannten Korrelationen für den nicht reaktiven Stofftransfer und den Enhancement Factor verglichen. Danach werden Regressionsalgorithmen aus dem Bereich des machine learning implementiert und auf dem Datensatz trainiert und ihre Performance bewertet. Ein trainierter Algorithmus wird daraufhin verwendet, um den Stoffaustausch und die daraus resultierende Volumenänderung einer aufsteigenden CO_2 Blase in Wasser zu simulieren. Der Einfluss des konjugierten Stoffaustauschs wird analysiert und die Ergebnisse mit experimentellen Daten verglichen.

Contents

0 Nomenclature

Dimensionless Groups

C	Courant number	$U\Delta t/\Delta x$
Da	Damköhler number	$kd_b c_i/u$
E	enhancement factor	Sh_i/Sh_{phy}
E_i	enhancement factor for instantaneous reaction	
H	dimensionless Henry coefficient	c_i^d/c_i^c
Ha	Hatta number	$\sqrt{k_{ij}D_i c_j}/\beta_{phy}$
Pe	Peclet number	$Re \cdot Sc$
Re	Reynolds number	Ud_b/ν
Sc	Schmidt number	ν/D
Sh	Sherwood number	$\beta d_b/D$

If not further specified the dimensionless number is calculated for the transfer species A.

Roman Symbols

A	transfer species	
B	bulk species	
C	second bulk species	
c	molar concentration	mol/m^3
C_D	drag coefficient	
D	diffusivity	m^2/s
F	force	$kg\ m/s^2$
g	gravitational constant	$9.81 m/s^2$
k	reaction rate constant	depending on reaction
n	normal	m
N	number of data points	
N	amount of substance	mol
p	pressure	$kg/(m\ s^2)$
P	product species	
u	velocity	m/s
r	radius	m
r	source term	$mol/(m^3 s)$
R	gas constant	$8.3144598 kg\ m^2/(s^2 mol\ K)$
R^2	R^2 score	
S	side product species	
t	time	s
w	polynom coefficients (weights)	
x	distance	m
X	molar fraction	

Greek Symbols

α	stoichiometric coefficient of rectands	
β	stoichiometric coefficient of products	
β	mass transfer coefficient	m/s
δ	Kronecker delta	
δ_c	concentration boundary layer thickness	m
η	dynamic viscosity	$kg/(m\ s)$
ν	kinematic viscosity	m^2/s
ν	components of stoichiometric matrix	
κ	eccentricity of the particle	
ρ	density	kg/m^3
τ	components of viscous stress tensor	$kg/(m\ s^2)$

Subscrips

b	bubble, used for bubble radius or diameter r_b,d_b
b	buoyancy
cf	creeping flow
conjugated	volume change with conjugated mass transfer
D	drag
hydro	simulated hydrodynamics
ideal	volume change without conjugated mass transfer
e	estimators
o	outer boundary
phy	physical mass transfer
r	radial direction
i	species i, sometimes also used for coordinate i
s	training samples
Σ	gas-liquid interface
Sp	specific gas constant
∞	far field of continuous phase

Superscrips

d	dispersed phase
c	continuous phase
j	j-th timestep
$+$	dimensionless

Other Symbols

Var(y)	variance of y

Acronyms

CFD	Computational Fluid Dynamics
DNS	Direct Numerical Simulation
KRR	Kernel Ridge Regression
MSE	Mean Square Error
SVR	Support Vector Regression
VoF	Volume-of-Fluid method

1 Introduction

Bubbles can be observed in a variety of technical applications, as well as in daily live. From opening a bottle of sparkling water, beer brewing or the mixing of multi fluid drinks, like "Laternsche", industrial processes like glass production, to a large variety of chemical and biochemical reactors, bubbles play a crucial role. Reactors and fermenters for example, rely on bubbles to mix liquid and gas components so that reactions can take place. The pharmaceutical industry relies on bubbles in the antibody, protein or hormone synthesis. To illustrate the importance of this topic the chemical industry had sales of 146127604 tsd.€ in 2015 [Bun17]. As stated in [Mar+11] reactions in multiphase gas–liquid flows make up 25% of all reactions taking place in the chemical industry, thus a better understanding of gas liquid interaction can have large implications for the chemical industry. But not only current industries could profit from a deeper understanding of bubble physics. As the pressure to reduce CO_2 emissions rises, new technologies for carbon capturing, bio fuels or livestock production are required. One promising technology for all these applications is the use of micro algal. These can be used to capture excess CO_2 from power plants, to produce bio fuels and the pharmaceutical industry can also implement them in many products due to their low toxicity. As micro algal are vastly grown in bubble column photobioreactors, improvements in the field of bubbly flows are needed as this technology is not profitable so far [HT11][CP17].
In most industrial reactors mentioned before the system is not only subject to two phase flow effects, but is further complicated by the presence of chemical reactions, which occur in most cases on time scales considered small compared to the movement of bubbles. Thus reactions take place in proximity to the gas liquid interface, leading to a strong coupling of mass transfer, bubble flow and reaction kinetics. Resulting from this coupling all three aspects are required to be analysed simultaneously to correctly predict or improve future reactor performance. In this context a major factor for rector performance is the mass transfer from gaseous to liquid phase. To accurately calculate the mass transfer computational fluid dynamics (CFD) is a useful tool. But since chemical reactions, bubble motion and flow patterns of reactors are present at length scales many orders of magnitude apart, a Direct Numerical Simulation (DNS) of all the phenomena would be infeasible considering current computational capabilities. To solve this problem scale reduced approaches like Euler-Euler or Euler-Lagrange simulations can be used to investigate entire reactors. These just simulate the larger scales, while smaller scales are modeled. For such models the physics at these scales must first be understood and modeled correctly.
As first step towards such a model the mass transfer at single bubbles needs to be analysed. Therefore, this thesis simulates the mass transfer at spherical gas bubbles and accesses the capabilities of known correlations and machine learning algorithms for the construction of surrogate models which then could be used in scale reduced methods. Because of the vast variety of applications, there are many publications discussing the physics of dispersed particles in fluids. Because the scope of this thesis is the development of a model to predict reactive mass transfer from spherical bubbles, only work on reactive mass transfer or relevant hydrodynamics are considered. In [CG78] the work on bubbles, drops and particles in continuous fluids until 1978 is compiled. For the description of flow fields around bubbles in creeping flow, an analytical solution was derived by Hadamard and Rybzynski independently. Another solution for creeping flows was found by Satapathy and Smith [SS60], who considered an outer wall at finite distance as domain boundary. This solution will be used in this thesis to calculate the convective species transport for creeping flows.
By using film theory Van Krevelen and Hoftijzer [VH48] were able to derive an expression for the en-

hancement factor, for gas liquid interfaces, one of the possible applications being bubbles. Discoursey [Dis74] found a similar expression using renewal theory. Both expressions build on the model of Danckwert [Dan70]. Additionally, Hikita and Asai found an expression for the enhancement using penetration theory, which also relies on the model of Danckwert [HA64].
In [GFB16] a subgrid model is used to simulate reactive mass transfer around a 3D bubble using a volume of fluid method (VoF). They found that the transfer rates at the bubble rear are enhanced, due to higher conversion rates in the bubble wake. This was also found by Khinast, Koynov, and Leib who simulated the reactive transfer rates with a fixed bubble model similar to the one used here. Furthermore, they found that film theory over-predicts the enhancement-factor, as the underlying assumption of a uniform boundary layer thickness is not met [KKL03].
In [Khi05] a number of different simulations is carried ot to evaluate the effect of bubble swarms on mass transfer. The influence of the Henry coefficient on mass transfers at spheres accompanied by a first order chemical reaction is studied in [Jun02]. The study is carried out only for a Peclet number of 100. In [Jun11] and [Jun12] the Henry coefficient and its influence on volume change of binary gas bubbles is depicted. While in [Jun11] the influence of the Reynolds number is compared to the analytical solutions for creeping flow and potential flow fields, in [Jun12] only creeping flows are considered but also the effects of a first order reaction taking place in the liquid phase are analysed. In both publications Peclet numbers up to 10^4 are taken into account. In [NHB16] and [Mer+17] the volume change of a rising CO_2 bubble in a water column is measured using optical instruments. While in [NHB16] the water is tapwater the experiment in [Mer+17] is carried out in degassed water. Both experiments show non vanishing bubble volumes.
In this thesis the reactive mass transfer at spherical gas bubbles is analysed. First an OpenFOAM model of the bubble is implemented. Afterwards simulations with varying dimensionless quantities in the range of $0 < Re < 100$, $10^4 < Pe < 10^6$ and $0 < Da < 10$ are carried out for four different reaction types. Since many data points are required only a fixed bubble model is used. First these results are compared to known correlations and the impact of different variables is discussed. Then data driven learning algorithms are trained to predict the Sherwood number based on the data points provided by the simulations. These algorithms are then compared in terms of prediction speed and accuracy. With these the conjugated mass transfer from a spherical bubble with changing volume is simulated. In chapter 2 the differential equations and boundary conditions which are needed to describe reactive mass transfer are presented. Boundary conditions are discussed and the equations are made dimensionless. From these equations the main parameters to describe the mass transfer, are selected. In chapter 3 machine learning is introduced and the later evaluated algorithms are presented. Afterwards the metrics and methods of evaluation and training are explained. Chapter 4 showcases the setup of the simulations needed for data generation. Afterwards in chapter 5 the obtained data is compared to known correlations for physical and reactive mass transfer. The effect of different flow fields is determined. Then the machine learning algorithms are trained and analyzed in terms of accuracy and prediction speed. Afterwards the algorithms are used to predict the transient behaviour of the bubble volume. The Thesis ends in chapter 6 with conclusion and an outlook.

2 Governing Equations

2.1 Problem Description

In the following chapter the used model for the simulation will be derived. Fluid flow and species transport would be simulated in the bulk and dispersed phase, but here only the continuous phase is simulated, because the diffusivities in gases are many orders of magnitude higher than those in liquids, such that the transfer resistances on the gaseous side of the interface is small and has little impact on the overall transfer rates. Additionally, it is assumed that the inside of the bubble is perfectly mixed and has a constant concentration. Furthermore, it is assumed that the flow is rotationally symmetric, since only low Reynolds numbers are tested. With these two simplification the domain can be reduced to a wedge of 2° without the bubble. The interface is introduced as boundary, as shown in figure 1.

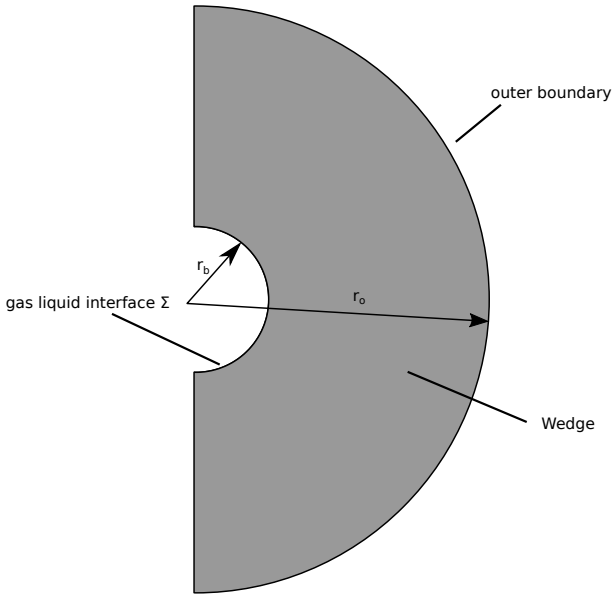

Figure 1: Domain wedge of 2° in sideview with boundaries.

2.2 Differential Equations and Boundary Conditions

The transport of dilute chemical species is described by the equation

$$\frac{\partial c_i}{\partial t} + \frac{\partial}{\partial x_j}(u_j c_i) - \frac{\partial}{\partial x_j}(D_i \frac{\partial c_i}{\partial x_j}) = r_i \quad , \tag{2.1}$$

where c_i is the molar-concentration of species i, u_j being the jth component of the velocity vector and D_i is the diffusivity of species i. The source term r_i accounts for the change of component i due to chemical reactions. Diffusive fluxes are modelled by Fick's law, as only diluted species are considered.
At the outer domain boundary it is assumed that the bulk phase continuous. Therefore, on the outer boundary,

$$\frac{\partial c_i}{\partial n_r}|_{r=r_o} = 0 \tag{2.2}$$

is set. The vector component n_r is pointing in radial direction. This condition is only valid, if far away from the field of interest, leading to domains spanning many bubble radii. At the inner boundary or interface Σ at $r = r_b$, the concentration would change between liquid and gaseous phase. To model the concentration on Σ in dependency of the concentration inside the bubble the dimensionless Henry coefficient,

$$H_i = \frac{c^d_{i,\Sigma}}{c^c_{i,\Sigma}} \tag{2.3}$$

is used. The one sided concentration limit at Σ from the dispersed phase is denoted as $c^d_{i,\Sigma}$, while $c^c_{i,\Sigma}$ is the concentration limit on the continuous phase. As already mentioned the concentration inside the bubble is constant in space and time, which leads to a constant value of $c^c_{i,\Sigma}$ on the interface. For convenience these are set to,

$$c^c_{i,\Sigma} = 1\frac{mol}{m^3} \quad \text{for the transfer species A} \tag{2.4}$$

$$c^c_{i,\Sigma} = 0\frac{mol}{m^3} \quad \text{for all other species} \quad . \tag{2.5}$$

Before solving (2.1) for the concentration fields, also the velocity components u_j must be known to model the convective term in (2.1). Therefore, the Navier-Stokes Equations must be solved.

$$\frac{\partial \rho}{\partial t} + \rho \frac{\partial u_i}{\partial x_i} = 0 \tag{2.6}$$

$$\frac{\partial}{\partial t}(\rho u_i) + \frac{\partial}{\partial x_j}(\rho u_i u_j) = \rho k_i + \frac{\partial}{\partial x_j}\tau_{ji} \tag{2.7}$$

Here the ρ is the density, k_i are the body forces and τ_{ij} are the components of the viscous stress tensor. As only incompressible, isothermal Newtonian Fluids are considered the conservation of mass can be simplified, since $\frac{\partial \rho}{\partial t} = 0$ for incompressible fluids, to

$$\frac{\partial u_i}{\partial x_i} = 0 \quad . \tag{2.8}$$

Additionally, τ_{ij} for isothermal Newonian Fluids is defined as

$$\tau_{ij} = -p\delta_{ij} + \eta(\frac{\partial u_i}{x_j} + \frac{\partial u_j}{x_i}) \quad , \tag{2.9}$$

where η is the dynamic viscosity. Because a fixed bubble model is used and only the steady state is viewed, body forces and transient terms can be neglected. Combining equation (2.6), (2.8) and (2.9) now leads to

$$u_j \frac{\partial u_i}{\partial x_j} = \frac{1}{\rho}\frac{\partial p}{\partial x_i} + \upsilon \frac{\partial^2 u_i}{\partial x_j \partial x_j} \quad , \tag{2.10}$$

where υ is the kinematic viscosity, defined as $\upsilon = \eta/\rho$. For p the boundary condition at the interface and the outer boundary are set to

$$\frac{\partial p}{\partial n_r}|_{r=r_b/r=r_o} = 0 \quad , \tag{2.11}$$

where n_r denotes again the radial direction. On the outer boundary the velocity vector $\underline{u}$ flows into and out of the domain. Therefore, the condition is either a fixed value for $\underline{u}$ if the vector points into the domain, or otherwise a zero gradient condition

$$\frac{\partial u_i}{\partial n_r}|_{r=r_o} = 0 \quad . \tag{2.12}$$

At the interface two conditions must be met. First the flow can not penetrate into the bubble so the velocity in normal direction to the interface must be zero.

$$u_r|_{r=r_b} = 0 \tag{2.13}$$

Additionally, the shear forces from the liquid onto the gas phase and vise versa must be identical. But because of the huge differences in viscosity the force onto the liquid would be small compared to the other effects in the continuous phase. Thus the experienced shear force on the interface is set to zero. For the simulations the velocity field is derived by solving equation (2.10). For the solutions in creeping flow fields the solution of Satapathy and Smith [SS60] is used to compute a velocity field which is then mapped onto the domain where species transport is solved.

2.3 Reactiontypes

In the previous chapter chemical reactions and their effect on the species conservation in equation (2.1) is accounted for by the source term r_i. For a system of n Species the j-th reaction can be described by

$$\alpha_{1j}A_1 + \alpha_{2j}A_2 + ...\alpha_{nj}A_n \longrightarrow \beta_{1j}A_1 + \beta_{2j}A_2 + ...\beta_{nj}A_n \tag{2.14}$$

with α_{ij} and β_{ij} being the stoichiometric coefficients of reactants and products, respectively. With these the rate function for the j-th reaction is defined as

$$r_j = k_j \prod_{i=1}^{n} c_i^{a_{ij}} \quad , \tag{2.15}$$

where k_j is the reaction rate constant of the j-th reaction and c_i is the concentration of species i. For species i the rate of change can now be defined as

$$\dot{c_i} = \sum_{j=1}^{m}(\beta_{ij} - \alpha_{ij})r_j = \sum_{j=1}^{m}\nu_{ij}k_j \prod_{i=1}^{n} c_i^{a_{ij}} \tag{2.16}$$

using the stoichiometric matrix $\beta_{ij} - \alpha_{ij} = \nu_{ij}$, and m being the number of reactions. From equation (2.16) an expression for the source term of species i can be derived.

$$r_i = \sum_{j=1}^{m} \nu_{ij} r_j = \pm \sum_{j=1}^{m} r_j = \pm \sum_{j=1}^{m} k_j \prod_{i=1}^{n} c_i^{a_{ij}} \tag{2.17}$$

Because only reactions with $\nu_{ij} = 1$ or $\nu_{ij} = -1$ for products and rectands respectively are considered in this thesis, the source term can be expressed as shown in (2.17). In the following the different reaction types and corresponding source terms are explained.

single Reaction

The single Reaction is defined as,

$$A + B \longrightarrow P \quad , \tag{2.18}$$

where A is the transfer species which diffuses from the bubble into the fluid and reacts with the bulk species B to P. The source term r_i follows,

$$r_i = \pm r_1 = \pm k\, c_A c_B \quad . \tag{2.19}$$

decay Reaction

The decay Reaction is a simplification of the single Reaction, defined as

$$A \longrightarrow P \quad , \tag{2.20}$$

where A is the transfer species which diffuses from the bubble into the fluid and reacts to P. If a single Reaction occurs while c_B remains nearly constant because it is present at larger quantities than needed for the reaction only decay reaction characteristics can be observed. The source term can be modelled as

$$r_i = \pm r_1 = \pm k\, c_A \quad . \tag{2.21}$$

parallel Competitive Reaction

The parallel competitive reaction consists of two single Reactions which can occur simultaneously.

$$A + B \longrightarrow P \quad \& \quad A + C \longrightarrow S \quad , \tag{2.22}$$

where B and C are both bulk species and S a side product. The source term is now just the sum of the relevant rate functions r_j.

parallel Consecutive Reaction

The consecutive reaction consists of two single reactions which occur consecutively.

$$A + B \longrightarrow P \quad \& \quad A + P \longrightarrow S \tag{2.23}$$

As well as the competitive reaction the consecutive one is build by implementing two single reactions, where the second one can only take place after the first one.

2.4 Dimensionless Quantities

2.4.1 Reynolds Number

The Reynold number is a dimensionless quantity, describing the ratio between inertia and viscous forces. It is used to compare flows patters. If the Reynolds number for two flows are equal and the shapes are just scaled, the flow fields are as well scaled versions of each other. The Reynolds number is defined as

$$Re = \frac{UL}{\upsilon} = \frac{Ud_b}{\upsilon} \tag{2.24}$$

With U being the characteristic velocity, L the characteristic length, in this case the bubble diameter d_b and υ being the kinematic viscosity of the fluid.

2.4.2 Schmidt Number

The Schmidt number is defined as the ratio of momentum diffusion to mass diffusion.

$$Sc = \frac{\upsilon}{D} \tag{2.25}$$

The kinematic viscosity was already needed for Re, while D is the diffusivity of a diluted species in the bulk fluid. The Schmidt number is a measure for the relative size of the concentration boundary layer in comparison to the hydrodynamic boundary layer. For high Schmidt numbers, as encountered in bubbly flow, the concentration boundary layer is deeply embedded in the momentum boundary layer.

2.4.3 Peclet Number

The Peclet nummer is the product of Re and Sc.

$$Pe = Re \cdot Sc = \frac{Ud_b}{\upsilon}\frac{\upsilon}{D} = \frac{Ud_b}{D} \tag{2.26}$$

It defines the ratio of convective to diffusive species transport. In many multiphase reactors the Peclet number is of $O(10^5)$, which is why in this thesis the Peclet numbers between 10^4 and 10^6 are analyzed. Resulting from these large values the mass transfer is dominated by convection.

2.4.4 Damköhler Number

This quantity was developed by Gerhard Damköhler. It is defined as the ration between reaction rate and convective species transport.

$$Da_i = \frac{k d_b c_{i0}^{n-1}}{U} \tag{2.27}$$

Here c_{i0} is the concentration of species i at either the interface for transfer species or far away from it for the bulk species, while n is the order of reaction for species i and k being the reaction rate constant.

2.4.5 Sherwood Number

The Sherwood number is a measure for the species transfer rate. It is used to calculate the mass transfer coefficient β. They are related by the expression (2.28).

$$Sh = \frac{\beta d_b}{D} \tag{2.28}$$

To extract the sherwood number from simulations the definition

$$Sh_{loc} = -\frac{\partial c_i}{\partial n_\Sigma} \Big/ \frac{c_\Sigma - c_\infty}{d_b} \tag{2.29}$$

for the local Sherwood-number is used. Afterwards, the area-weighted integral of Sh_{loc} over the interface is taken, to compute the global Sherwood number. (2.30). [Fle14]

$$Sh = \frac{1}{|\partial V|} \int_{\partial V} Sh_{loc} dA \tag{2.30}$$

Finding easy expressions for Sh as a function of Pe, Re and Da, as well as verifying existing correlations is one of the goals of this thesis.

2.5 Governing Parameters

So far equation(2.1) and (2.10) describe the relevant physical phenomena. For machine learning algorithms, however, it is now required to chose relevant parameters, which can or could have an influence on the mass transfer. Rise velocity and bubble diameter, for example, are present in the equations and could be used as parameters, but as each new parameter adds complexity to the problem, the least possible number of parameters should be used. Therefore, both equations are made dimensionless by using

$$c_i^+ = \frac{c_i}{c_{i0}} \tag{2.31}$$

$$u_i^+ = \frac{u_i}{U} \tag{2.32}$$

$$p^+ = \frac{p}{\rho U^2} \tag{2.33}$$

$$x_i^+ = \frac{x_i}{d_b} \tag{2.34}$$

$$t^+ = t\frac{U}{d_b} \tag{2.35}$$

$$r_i^+ = \pm c_i^+ \text{ for decay reaction} \tag{2.36}$$

$$r_i^+ = \pm c_i^+ c_j^+ \text{ for single reaction} \quad , \tag{2.37}$$

resulting in

$$\frac{\partial c_i^+}{\partial t^+} + \frac{\partial u_j^+ c_i^+}{\partial x_j^+} - \frac{1}{Pe_i}\frac{\partial^2 c_i^+}{\partial x_k^+ \partial x_j^+} = Da_i r_i^+ \tag{2.38}$$

$$u_j^+ \frac{\partial u_i^+}{\partial x_j^+} = \frac{\partial p^+}{\partial x_i^+} + \frac{1}{Re}\frac{\partial^2 u_i^+}{\partial x_j^+ \partial x_j^+} \quad . \tag{2.39}$$

By using only variables still present in these equations the parameter space can be drastically reduced as now, for example, the features d_b,η and U all collapsed into Re.

2.5.1 Decay Reaction

Using the dimensionless equation introduced above, the decay Reaction can be described by

$$\frac{\partial c_A^+}{\partial t^+} + \frac{\partial u_j^+ c_A^+}{\partial x_j^+} - \frac{1}{Pe_A}\frac{\partial^2 c_A^+}{\partial x_k^+ \partial x_j^+} = Da_A r_A^+ \tag{2.40}$$

$$\frac{\partial c_P^+}{\partial t^+} + \frac{\partial u_j^+ c_P^+}{\partial x_j^+} - \frac{1}{Pe_P}\frac{\partial^2 c_P^+}{\partial x_k^+ \partial x_j^+} = Da_P r_P^+ \tag{2.41}$$

$$\tag{2.42}$$

From these set of equations, 3 features can be derived. First the Reynolds number as u^+ is a function of Re. The Peclet number for species A and the Damköhler number as they directly influence species

transport. The Peclet number for species P is not of interest, as the presence of P has no further effect on the transfer rates.

2.5.2 Single Reaction

The single reaction introduces another species equation for the bulk species B.

$$\frac{\partial c_A^+}{\partial t^+} + \frac{\partial u_j^+ c_A^+}{\partial x_j^+} - \frac{1}{Pe_A}\frac{\partial^2 c_A^+}{\partial x_k^+ \partial x_j^+} = Da_A r_A^+ \tag{2.43}$$

$$\frac{\partial c_B^+}{\partial t^+} + \frac{\partial u_j^+ c_B^+}{\partial x_j^+} - \frac{1}{Pe_B}\frac{\partial^2 c_B^+}{\partial x_k^+ \partial x_j^+} = Da_B r_B^+ \tag{2.44}$$

$$\frac{\partial c_P^+}{\partial t^+} + \frac{\partial u_j^+ c_P^+}{\partial x_j^+} - \frac{1}{Pe_P}\frac{\partial^2 c_P^+}{\partial x_k^+ \partial x_j^+} = Da_P r_P^+ \tag{2.45}$$

$$\tag{2.46}$$

Besides Re, Pe_A and Da, two additional features are introduced. First the Peclet number for species B and second the ratio of the concentrations of B far from the interface to A at the interface. To reduce the possibility of confusion in the following Pe is always the Peclet number for the transfer species A, and instead of using Peclet numbers of species B the ratio of diffusivity is used, which is the same as the ratio of Pe, as $Pe = Re \cdot \upsilon/D$ and $Re \cdot \upsilon = const.$ since both species are dilute and have no impact on the viscosity.

2.5.3 Parallel Competitive Reaction

In the competitive reaction two more equations are added.

$$\frac{\partial c_C^+}{\partial t^+} + \frac{\partial u_j^+ c_C^+}{\partial x_j^+} - \frac{1}{Pe_C}\frac{\partial^2 c_C^+}{\partial x_k^+ \partial x_j^+} = Da_C r_C^+ \tag{2.47}$$

$$\frac{\partial c_S^+}{\partial t^+} + \frac{\partial u_j^+ c_S^+}{\partial x_j^+} - \frac{1}{Pe_S}\frac{\partial^2 c_S^+}{\partial x_k^+ \partial x_j^+} = Da_S r_S^+ \tag{2.48}$$

As in the case of single or decay reaction the equation for the side product S has no further impact on the system. To capture the influence of species C, as for the introduction of species B in the single Reaction, D_C/D_A and c_C/c_A are added as parameters. Furthermore, since now two reactions take place an additional Damköhler number Da_{AC} is needed to describe the second reaction.

2.5.4 Parallel Consecutive Reaction

In the consecutive reaction the second reaction takes place between A and P, so that no species C is needed. So the features that are added in comparison to the single reactions are D_P/D_A and Da_{AP}. Because P is first produced by the reaction no feature for the concentration of P is needed.

3 Machine Learning

3.1 Workflow

Machine learning, a field of artificial intelligence, uses algorithms to make predictions based on data. It can be divided into 3 different learning types, namely unsupervised, supervised and reinforcement learning. Because only supervised learning is used, the other two wont be discussed here. The reader is refered to the literature for more information [Ras15].
The scope of machine learning algorithms is to correctly predict a target value, in this case the Sherwood number, when a set of input variables is given. In the context of machine learning the input and output parameters are called features and target variables, respectively. In supervised learning the algorithm is trained by a set of given features and corresponding target variables, which can either be discrete or continuous as in our example. If the target variable is discrete the problem is called classification and the target is also refered to as label, otherwise the term regression is used. In this thesis only regression models with continuous features are used. The algorithm is trained by changing parameters inside the algorithm until the difference between predictions and known target is minimal. In figure 2 the described work flow is shown. First a set of features and target variables is produced using direct numerical simulations of bubbles. This set is then divided into a train and test set, containing 90% and 10% of all points, respectively. The larger set is used to train the data, while the other one is later used to determine the capability of the model via the R^2 metric, which will be defined in (3.5). Splitting the data is necessary, because the algorithm might recognize the training set perfectly, but is unable to generalize to new data, which is why a second set for evaluation is needed. Besides this accuracy rating it is evaluated how well the algorithm scores in comparison to the amount of training data, and how fast they make predictions. For

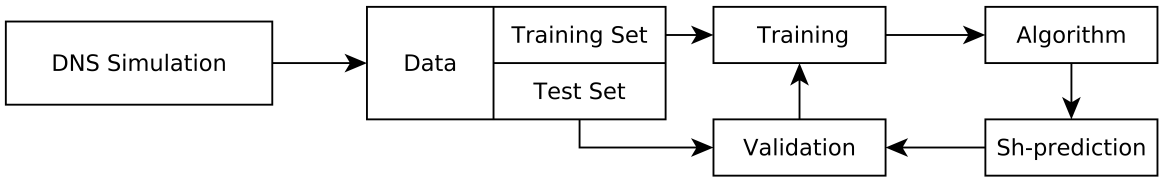

Figure 2: Overview of the workflow used to train the machine learning algorithms.

this thesis the algorithms are taken from the scikit-learn environment in Python. For more information on the software and algorithms the reader is refered to [Ped+11] or their homepage [Ped+17a]. In the following some suitable algorithms are presented. The information is taken from the scikit-learn homepage [Ped+17a]. More detailed information on the algorithms can also be found there.
Note that, since the numerical simulations are deterministic, interpolation could also be used to learn from the data. This however, would fail in the case of experimental results, as they are subjected to random noise, which would make interpolation impossible. Therefore, to later be able to use the same approach for experimental and numerical data, only regression models are tested.

3.2 Algorithms

3.2.1 Linear Regression

Linear regression is the prediction of the target value by the assumption that the target is a linear superposition of the input variables of the form

$$y(x_1, x_2, ..., x_n) = w_0 + w_1 x_1 + w_2 x_2 + ... + w_n x_n \quad . \tag{3.1}$$

The weights w are typically calculated by minimizing the squared error.

$$\min_R \parallel (\underline{X} \cdot \underline{w} - \underline{y}) \parallel^2 = R \tag{3.2}$$

The optimal values for the weights w is found via optimisation algorithms implemented in scikit-learn. As it requires only simple multiplications and additions the algorithms are able to make fast predictions which is a key for the implementation in scale-up applications, as they require a large number of predictions per second to be feasible. To capture non linear trends in the data polynomials can be used in the same way as linear regression.

$$y(x) = w_0 + w_1 x + w_2 x^2 + ...w_d x^n \tag{3.3}$$

Note, that this is still a linear regression, as the variables $x, x^2, x^3..., x^d$ can be transformed to $z_1, z_2, z_3, ..., z_d$. With increasing number of weights trends of higher order can be fitted, but the prediction latency also increases exponentially with the power of the polynom. One problem of this approach is that correlated features, which is the case for the polynomial regression, leads to unstable optimisation. To mitigate this problem the ridge regression is used which introduces an additional penalty for the size of the weights, as seen in (3.4).

$$\min_R \parallel (\underline{X}\,\underline{w} - \underline{y}) \parallel^2 + \alpha \parallel \underline{w} \parallel^2 = R \tag{3.4}$$

The penalty is controlled via the α parameter. Linear regression alone can not be used in this thesis as the data is non linear. Therefore, it is required to transform the features into a polynomial input. As the coefficients can be printed the results can also be used outside python. More complex data might require a polynom of higher order. Since the prediction time scales exponentially with the polynom order, this approach might be impractical for complex systems. As the features are up to seven orders of magnitude apart from each other a scaling of the input features to range from [0,1] is used, as otherwise the weights w might not converge properly, because of the huge scale difference.

3.2.2 Decision Tree and Random Forest Regression

Decision Trees build step functions that best fit the data provided, as shown in figure 3. This is done by applying a binary tree to the feature space, where each new node is a question which maximises information

gain. By the nature of this approach the prediction latency increases logarithmically [Ped+17b] with the number of training points provided, as this leads to larger trees and thus longer prediction times [Ras15, p. 304]. In addition to the classical decision tree random forest regression is tested. Here many smaller

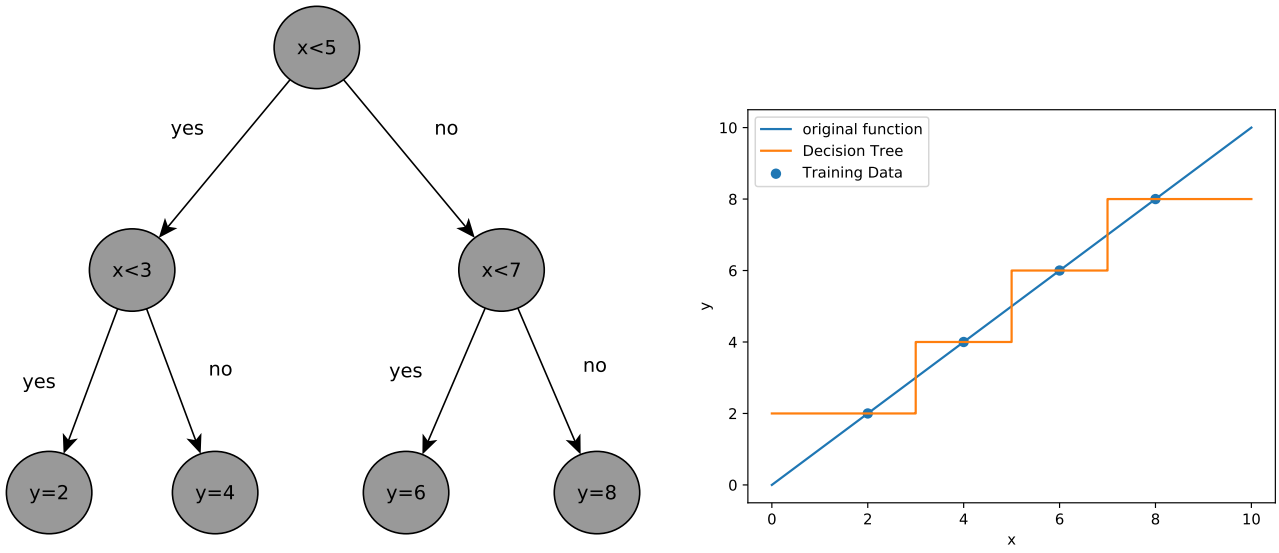

Figure 3: Binary decision tree(left) and corresponding regression for y=x (right), with training points at x=[2,4,6,8].

decision trees are trained on the data. For predictions the average answer of all trees in the forest is used. Furthermore, the trees in the forest are only trained on a subset of the training set and their generation is randomised. Decision trees do not need data transformation beforehand, but note that missing values still need to be purged. Also categorical features, such as 'bubble or particle' could easily be included. However, they are unstable as small changes in training data might lead to a different split early in the tree, leading to a completely different trees. Decision trees tend to over-fit the data, meaning that it often includes points which are subject to noise. This is of little concern in this context as the simulated data is not subject to noise, but if such models were trained on experimental data over-fitting could be an issue [Bel14]. Another problem arises from the regression form. As a decision tree is build from step functions it can not capture the continuous data trend. Some of these disadvantages are solved by random forests. They do not easily over-fit, since the law of large numbers applies, which states that the average of many decisions is better than a single one. This also reduces the variance of the prediction [Bre01]. Furthermore, random forests produce more steady regressions because of the averaging, which increases their score on continuous data like the one used here.

3.2.3 Kernel Based Algorithms

In this class of algorithms the features are transformed onto a higher dimensional space using the kernel trick. Afterwards a linear regression in this space is used to predict the target variable. This approach is mostly used for systems with a large number of input features. Two different types are used in this thesis, the Support Vector Regression (SVR) and the Kernel Ridge Regression (KRR). A ridge regression, as presented in (3.4), is used as linear model for KRR, while SVR uses the ordinary least square method.

Kernel based approaches are effective in high dimensional feature spaces, but they are not scale invariant, thus the input features must first be scaled to a range between [0,1], [-1,1] or standardized, meaning a transformation towards zero mean and a variance of one. In contrast to the other algorithms outlined here the inner workings of SVR and KRR are far more complex, resulting in a black-box system. On the other hand linear regression or tree based approaches can be visualised and easily understood. Because KRR uses a different loss function it is generally fitted faster than SVR [Ped+17a]. Another disadvantage of these algorithms is that they construct support vectors from the training data which are used to make the predictions. Because of that the prediction latency scales with the size of the training set. Furthermore, these support vectors lead to computationally expensive operations, as they are stored in the working memory.

3.3 Performance Analysis

To compare the different algorithms two factors are of importance. First the model must be able to make correct predictions. Therefore the R^2 metric can be used which is defined as the mean squared error (MSE) devided by the variance.

$$R^2 = 1 - \frac{MSE}{Var(y)} = 1 - \frac{\frac{1}{N_t}\sum_{i=1}^{N_t}(y^{(i)} - \hat{y}^{(i)})^2}{\frac{1}{N_t}\sum_{i=1}^{N_t}(y^{(i)} - \mu_y)^2} \tag{3.5}$$

MSE can be interpreted as the average distance or error between correct target value y and the predicted value $\hat{y}$ squared. R^2 is the transformation of this metric into a range of $[0; 1]$. Note that R^2 can be negative for data outside of the training set. If $R^2 = 1$ the model correctly predicts all data points [Ras15, p. 296]. The other criterion is the time needed to make predictions, which will be called prediction latency in the following sections. As the model should later be used in simulations to predict the species transfer in scale reduced simulations for each cell, millions of predictions per time steps are possible. As a result this approach is only applicable when the predictions can be made fast enough. The time required for training on the other hand is far less important, as it can be done prior to the simulations. There are two additional constraints. First the algorithm should need as few data points as possible to make accurate predictions, and second it should scale well with larger datasets, meaning that with increasing number of data points the accuracy should increase and the prediction latency should not change.

4 Numerical Setup

4.1 Overview

For solving the equations presented in Chapter 2.2 the OpenFoam software is used. For the hydrodynamics the simpleFoam solver is used, while the species transport is solved using a custom solver which uses the steady state flow field obtained by simpleFoam. For detailed information on the solver as well as the software itself, the OpenFoam Website offers a detailed documentation [Ltd17].
For creeping flow simulations the Satapathy solution is used [SS60]. From that the flux $\underline{phi}$ was evaluated using the custom utility 'satapathyVelocity'. Afterwards the species transport was simulated.
For the simulation with hydrodynamics two independent steps are carried out. As only the steady state is scope of this thesis the Navier-stokes-equations are first solved with the steady state solver simpleFoam. Afterwards all simulations with the same Reynolds number copy the $\underline{phi}$ field and solve the species transport on the same grid. The grid for the domain as shown in figure 1 is depicted from the side in figure 4, and is made up of prism cells. The wege angel is 2°.

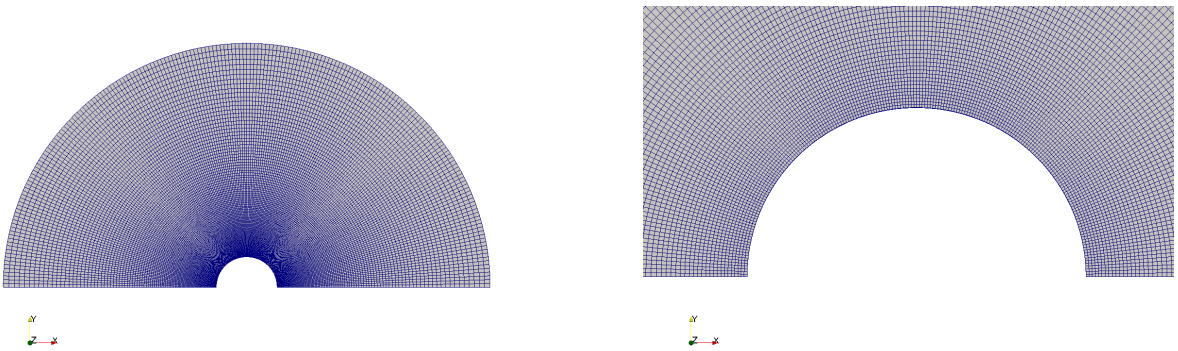

Figure 4: complete mesh (left) and enlarged view of the interface (right).

4.2 Setup

For the hydrodynamics equation (2.10) needs to be solved, so the flux field can be passed on to the species transport. For the simulations the dynamic viscosity of the bulk phase ν was set to $2 \cdot 10^{-6} m^2/s$. Note that while the density ρ still appears in equation (2.10). Because OpenFOAM already calculates with p normalised by the density no value for ρ must be given. The boundary condition for $\underline{U}$, p and the concentration fields c_i derived in chapter 2 are integrated by the OpenFOAM conditions in table 1.
The schemes used for this simulation can be found in table 2. The simulation ran until the convergence

boundary	condition U	condition p	chemical species c_i
outer	inletOutlet	zeroGradient	zeroGradient
interface	slip	zeroGradient	fixedValue
radial cut	wedge	wedge	wedge

Table 1: boundary conditions used in the simulations.

schemes	type
ddt schemes	steadyState
gradSchemes	Gauss linear
divSchemes	Gauss linear
laplacianSchemes	Gauss linear corrected
interpolationSchemes	linear
snGradSchemes	corrected

Table 2: Schemes used to solve the momentum equation.

criteria for the residuals for $\underline{U}$ and p was reached, which were set to 10^{-3} and 10^{-4}, respectively. For species transport the custom solver reactingSpeciesFoam is used, solving equation (2.1), with (2.17) for the source term. For the specified boundary conditions in chapter 2, OpenFOAM specific conditions are used which can also be found in table 1. The numerical schemes used are presented in figure 3. As this

schemes	type
ddt schemes	Euler
gradSchemes	Gauss linear
divSchemes	Gauss limitedLinear 1
laplacianSchemes	Gauss linear corrected
interpolationSchemes	linear
snGradSchemes	corrected

Table 3: Schemes used to solve the concentration fields.

simulation is transient, the size of the time step size must be considered. To define it the Courant number is used.

$$C = \frac{U\Delta t}{\Delta x} \tag{4.1}$$

Because the Courant number should be below 1 the timestep size is choosen by

$$\Delta t = \frac{\Delta x C}{U} = \frac{\Delta x}{U} \quad , \tag{4.2}$$

where Δx is the height of the first prism layer and U the characteristic velocity or rise velocity in this case. As both are known a priori the step size can be calculated directly.
The overall simulation time is set to $1500\Delta t$, as this was long enough for even the worst case, meaning lowest Damköhler, Reynold and Peclet number, to develop a steady state species transfer.

4.3 Mesh Dependency Study

To arrive at a grid independent solution a grid study was carried out using the domain shown in figure 1 and prism cells. As already stated in 2.4.2 the concentration boundary layer is some orders of magnitude smaller than the viscous boundary layer, leading to difficulties solving both systems on one grid, as it needs to be fine enough near the interface to capture the concentration layer. As grid convergence criteria

the Sherwood number is used. This only captures the grid convergence of species transport, but because this requires much finer grids it is assumed that if the grid is fine enough to capture the concentration boundary layer, the hydrodynamic solution also reached grid convergence, as it requires a coarser mesh. The different grids are tested by simulating a test case with $Re = 100$, $Pe = 10^6$ and $Da = 10$, since these lead to the smallest boundary layers and hence are most demanding in terms of mesh size. As a first estimation of the required cell size in proximity to the interface the thickness of the resulting concentration boundary layer needs be approximated. Therefore, the correlation $\delta_c \propto r_b(Pe)^{-1/2}$ for non-reactive mass

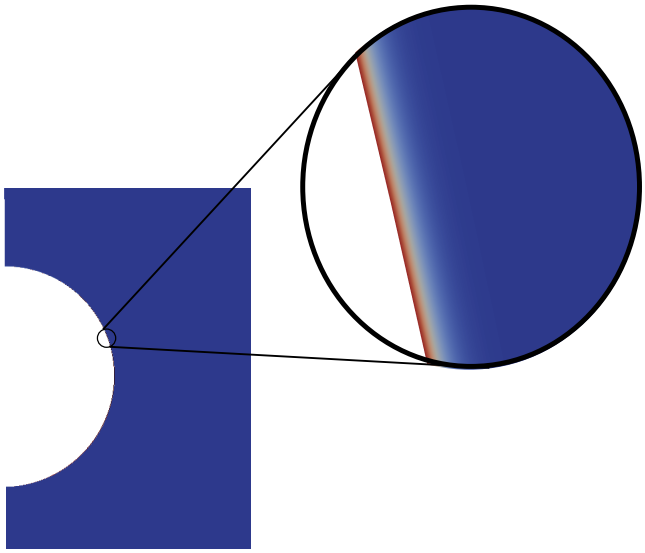

Figure 5: Simulated concentration boundary layer on bubble with 2mm diameter.

transfer as found in [HMD91] is used. For bubbles with a diameter of $2mm$ and the Peclet number ranging form 10^4 to 10^6 the boundary layer thickness is thus expected to vary between $20\mu m$ and $2\mu m$. Because the correlation is only applicable for physical mass transfer it is assumed that the actual thickness is even smaller. Therefore the grid study started with cell sizes at the interface of around $0.5\mu m$. In tabel 4 the grid studys for the simulations using the Satapathy solution are depicted. The relative change between

Nr.	Radial	Polar	Grading	Outer Radius	first Cell	Sh
1	125	150	0,01	$4 \cdot r_b$	$1.1\mu m$	2384
2	250	150	0,01	$4 \cdot r_b$	$0.55\mu m$	2900
3	500	150	0,01	$4 \cdot r_b$	$0.28\mu m$	3095
4	1000	150	0,01	$4 \cdot r_b$	$0.14\mu m$	3151

Table 4: Mesh convergence study using the Satapathy and Smith velocity field.

grid 3 and grid 2 is 6.7%, and 1.8% between grid 4 and grid 3, thus grid 3 is chosen.
For the case of simulated hydrodynamics, the outer boundary needs to be far away from the field of interest. Otherwise the boundary condition, in this case 'zero gradient' might influence the obtained solution, as it is not a good approximation near perturbations such as a bubble. Instead of increasing the cell count the grading was increased as countermeasure. Therefore, the cell size in the vicinity of the bubble is smaller than for grid 4 in 4, resulting in a smaller error. Furthermore, the influence of domain radius and the polar

cell count are tested as seen in table 5. For the study the second grid is used as more polar cells do not change the solution and the effects of a larger domain can also be neglected.

Nr.	Radial	Polar	Grading	Outer Radius	first Cell	Sh
1	500	300	0,001	$10 \cdot r_b$	$0.124 \mu m$	4499,57
2	500	150	0,001	$10 \cdot r_b$	$0.124 \mu m$	4502,58
3	600	300	0,001	$16 \cdot r_b$	$0.172 \mu m$	4459,64
4	600	400	0,001	$16 \cdot r_b$	$0.172 \mu m$	4460,26

Table 5: Mesh convergence study with simulated hydrodynamics.

4.4 Design of Experiment

To evaluate the behaviour of bubbles in the feature space two different distributions of simulations are used. First the simulations are spaced evenly over the feature space. This has the advantage, that the results can be easily evaluated by humans and can be used for visualisation as seen in chapter 5.1 and 5.2. For training purposes this field is at a disadvantage, since the data is presented in a certain order the algorithm might adopt not to the underlying trend, but to the spacing of the data points. Additionally, this would not be seen by testing the algorithm on the test set, since this set is also biased. Therefore, the simulations are also distributed randomly in the feature space in a Monte Carlo design [SBH, p. 42]. The algorithms are trained on these second set. The simulations are created automatically by a python script. As the different features are often dependent on the same variables there are multiple ways to arrive at a certain data point in the feature space. As the geometry can not be changed, since then a new numerical mesh would be needed the bubble diameter d_b remains constant. The viscosity of the bulk phase ν as well as the interface concentration c_A stayed constant as well. The Reynolds number was adjusted by changing the characteristic velocity U. As $Pe_A = Re\,\nu/D_A$ the Peclet number changed with the diffusivity of species A. The Damköhler number was manipulated using the reaction rate constant k_j. Note that Da also depends on the characteristic velocity. The other features are all ratios in dependency of either the diffusivity or the concentration of the transfer species A. Since the values for A were set by the other features the diffusivity or concentration of the other species was scaled accordingly. To reduce the risk of wrong data the program reading the data directly analyzed the openFoam dictionaries, thus ensuring that the data gathered after the simulation fits to the simulated parameters.

5 Results

5.1 Physical Species Transfer

In table 6 known correlations for physical mass transfer are compiled. The last two correlations do not

Research Group	Correlation
Takemura [TY98]	$Sh = \frac{2}{\sqrt{\pi}}[1 - \frac{2}{3}\frac{1}{(1+0.09Re^{2/3})^{3/4}}](\frac{2.5}{Pe^{1/2}} + Pe^{1/2})$
Lochiel [LC64]	$Sh = \frac{2}{\sqrt{\pi}}(1 - \frac{2.98}{Re^{1/2}})^{1/2}Pe^{1/2}$
potential flow solution [LC64]	$Sh = \frac{2}{\sqrt{\pi}}Pe^{1/2}$
Clift[CG78, p. 50]	$Sh = 0.65(\frac{Pe}{1-\kappa})^{1/2}$
Oellrich[OSB73]	$Sh = 2 + \frac{0.651Pe^{1.72}}{1+Pe^{1.22}}$

Table 6: correlations for Sherwood-numbers for non-reactive mass transfer as found in literature.

depend on the Reynolds number as they are derived for creeping flow conditions.The solution by Takemura and Yabe [TY98] is valid for low Reynolds numbers between 0.1 and 100 and Peclet numbers above 1. For Reynolds numbers below 30 the correlation of Takemura and Yabe predicts Sherwood number lower than the data obtained with the Satapathy field, thus this correlation should only be used for Reynold numbers above 30. Note that the equation is misprinted in the original publication. The corrected version was taken from [Fle14]. In Lochiel and Calderbanks publication [LC64] the correlation is derived based on penetration theory. For very high Reynolds numbers this equation converges towards the solution for potential flow. It is only valid for high Reynolds numbers and for Re>50 it is close to the solution of Takemura and Yabe. While the results of Takemura and Lochiel depend on the Reynolds number the simulations could not replicate this dependency in the study as shown in the heatmap in figure 6. A heatmap prints the covariance of two features divided by their standard deviation [Ras15, p. 283]. The result varies between -1 and 1, being either a perfect negative or perfect positive correlation. In figure 7 the Sherwood numbers for physical species transfer, as obtained from the simulations, are compared to the correlations from table 6. 'Data points' are simulation points obtained with the two step solver with simulated hydrodynamics, while 'Data creeping flow' is simulated with the Satapathy solution. All correlations for creeping flow agree well with the simulated results, while the correlations for $Re > 1$ depend on Re, which is not the case for the simulations. The simulations agree well with the solution for potential flow fields. Since the simulation of the hydrodynamics uses the slip condition at the interface it is close to the potential flow solution. Thus the influence of the changing Reynolds number can not be captured. For higher Reynolds numbers the correlations from Takemura and Lochiel predict the same Sherwood numbers, while for lower values of Re Lochiels correlation predicts lower values for the Sherwood number. From this it is assumed that the data over-predicts the species transfer as the influence of Re is not captured.

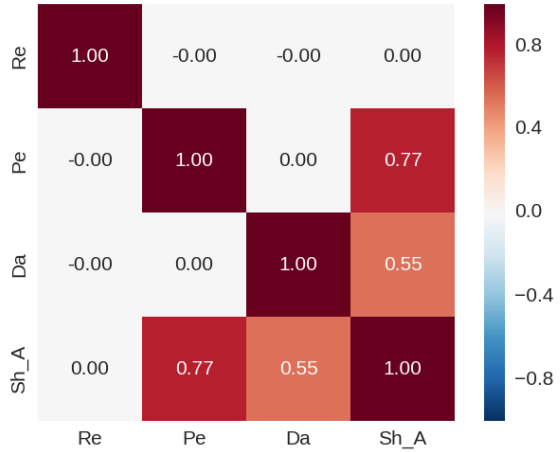

Figure 6: Heatmap for Decay Reaction with $Pe \in [1e^4; 1e^6], Re \in [2; 100], Da \in [0; 10]$.

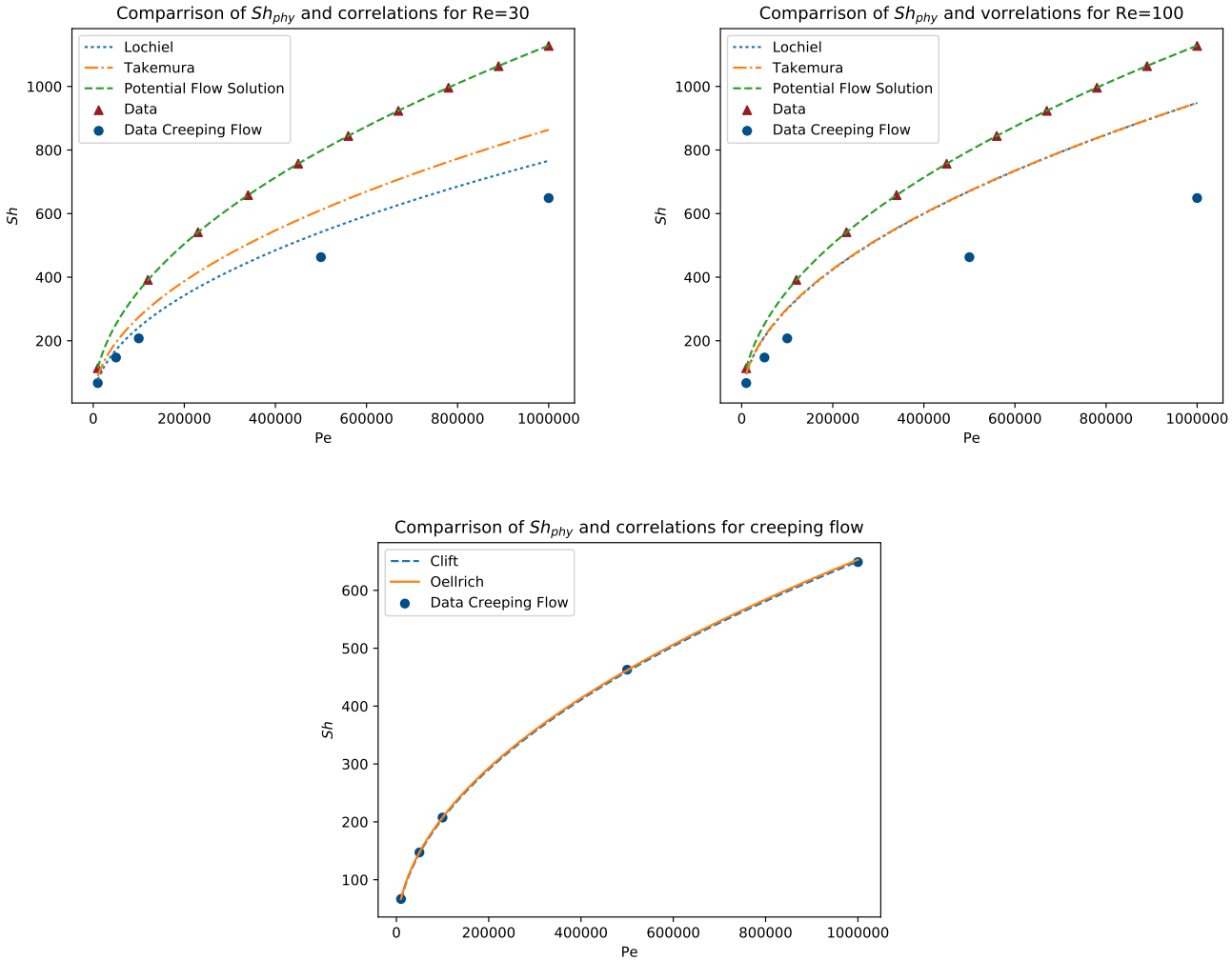

Figure 7: Comparison of Sh and known correlations with $Pe \in [1e^4; 1e^6]$, for higher Reynolds numbers (first two graphs), and creeping flows (lower graph).

5.2 Enhancment Faktors

The above section solely compared correlations for physical species transfer. For reactive species transfer no closed correlation is known. Instead the Enhancement-factor (E-factor) is used (5.1).

$$E = \frac{Sh}{Sh_{phy}} \tag{5.1}$$

The enhancement factor is the ratio of the reactive Sherwood-number to the one obtained with just physical species transfer. To access the relation between the features of the single reaction and E a heatmap is used (figure 8). Note that Re is no longer shown, as the simulations can not depict its influence. Only

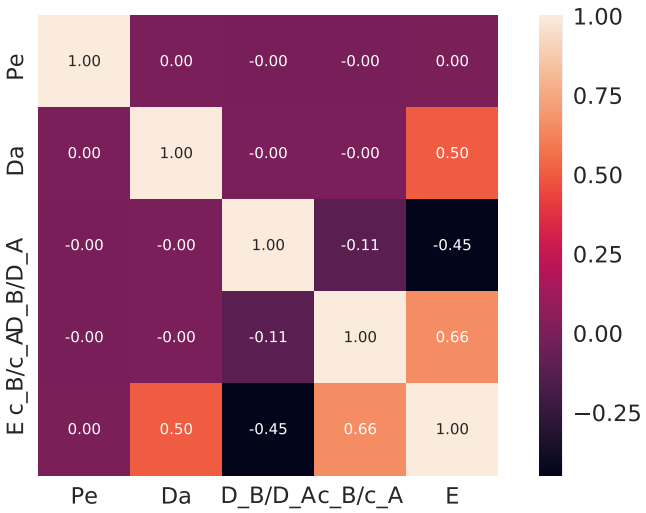

Figure 8: Heatmap for Enhancement factor with $Pe \in [1e^4; 1e^6]$, all other features are $\in [0.1; 10]$.

the bottom row is of interest as all other correlations are zero as their values are randomly assigned. The heatmap shows, that the enhancement does not depend on Pe. Only because this is the case it is possible to construct a model based on the physical mass transfer and use the enhancement to compute the reactive transfer rates. Another interesting finding is this that the enhancement factor decreases with larger values of D_B/D_A, as seen in the negative correlation in the graph (black tile). In the following three enhancement factor models are presented. All three of them are valid for single reactions.

Renewal Model

For a single reaction Discoursey found the correlation (5.2) [Dis74].

$$E = -\frac{Ha^2}{2(E_i - 1)} + \sqrt{\frac{Ha^4}{4(E_i - 1)^2} + E_i \frac{Ha^2}{(E_i - 1)} + 1} \tag{5.2}$$

Here Ha is the Hatta number, which compares reaction rates in a liquid film to the rate of diffusion. For a single reaction the Hatta number is defined in (5.3).

$$Ha = \frac{\sqrt{k_{AB} D_A c_B}}{\beta_{phy}} \tag{5.3}$$

The physical mass transfer coefficient β_{phy} could be calculated using a known correlation for the physical mass transfer, but for this study it is taken from the simulations, so no additional error is introduced. The enhancement for an instantaneous reaction E_i was proposed by Danckwert [Dan70] and is also used in (5.2).

$$E_i = \frac{1}{erf(\frac{\gamma}{\sqrt{D_A}})} = \frac{erf(\gamma/\sqrt{D_B})}{erf(\gamma/\sqrt{D_A})} + \frac{exp(\gamma^2/D_B)}{exp(\gamma^2/D_A)} \frac{c_{B\infty}}{\nu_B C_{A\Sigma}} \sqrt{\frac{D_B}{D_A}} \tag{5.4}$$

This expression needs to be estimated by numerical means. Only if $D_A = D_B$ an analytical solution becomes possible and (5.4) takes the form of (5.5) [KR17].

$$E_i = 1 + \frac{c_{B\infty}}{\nu_B c_{A\Sigma}} = 1 + \frac{c_{B\infty}}{c_{A\Sigma}} \tag{5.5}$$

For this thesis only the case for $D_A = D_B$ will be analyzed.

Film Model

Van Krevelen and Hoftijzer [VH48] found an expression for E using film theory.

$$E = \frac{Ha\,\eta}{\tanh(Ha\,\eta)} \tag{5.6}$$

with, $\eta = \sqrt{\frac{E_i - E}{E_i - 1}}$. As this is an implicit expression it is calculated numerically using a bi-section algorithm (see A.1). The start value is the result of the Renewal model.

Penetration Model

By using the penetration model Hikita and Asai [HA64] also found an implicit expression for E.

$$E = (Ha\,\eta + \frac{\pi}{8Ha\,\eta}) erf(\frac{2Ha\,\eta}{\sqrt{\pi}}) + 0.5 exp(-4\frac{4Ha^2\eta^2}{\pi}) \tag{5.7}$$

The code can be seen in A.1. As upper limit 0.95% of E_i and as lower limit 0.8% of the renewal result were taken, since in [KR17] it is shown that all three correlations predict nearly the same results. In figure 9 the results of the above mentioned correlations are compared to the simulation data. Note that the Hatta

number is computed from the physical mass transfer in the simulations and also depicted in the graphs. Also the relative difference $\Delta E = (E_{model} - E_{num})/E_{num}$ is shown on the right. The Hatta number ranges from 0.8 to 2.7. For concentration ratios of unity the correlations predict 20 to 25% (depending on the model) higher enhancement factors than the simulations, for high Damköhler numbers. The deviation is smaller for small Damköhler numbers. For smaller Damköhler numbers the three models predict different values, while for higher Damköhler numbers all three converge towards the same value. While for the concentration ratio of $c_B/c_A = 9$ this convergence value seems to be a maxima, the curves for lower concentration ratios have a maxima at about $Da = 5$. For growing concentration ratios the differences between the models becomes smaller. For concentration ratios of $c_B/c_A = 3$ the minimal encountered deviation is already 31% and the largest is about 60%. For $c_B/c_A = 9$ the minimal error is at 68% while they converge towards 1.1% for high Damköhler numbers. For concentration ratios of unity and a Damköhler number of one penetration theory only shows a deviation of 1.5%. As the relative difference converges towards a constant value the general correlation between Da and the enhancement curve seems to be captured. For all concentration ratios and Damköhler numbers the Renewal model always has the highest deviation. Note that, while this graphs are only printed for $Pe = 10^4$, the graph would look the same for any Peclet number, since, as shown in figure 8, the Peclet number has no influence on the enhancement factor.

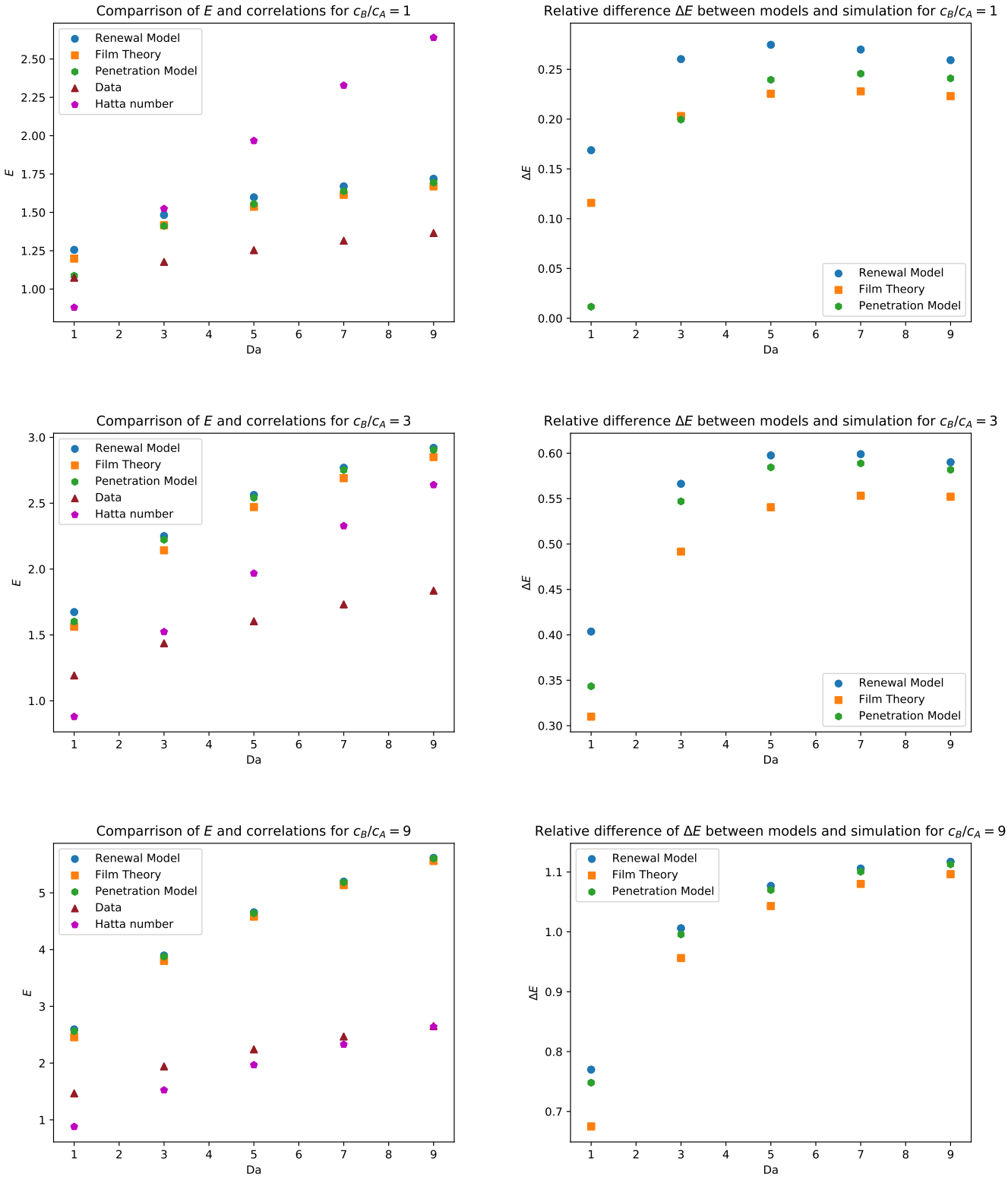

Figure 9: Comparison of E factors from different models and data points(left side) and the relative difference ΔE (right side) for different concentration ratios at $Pe = 10^4$.

5.3 Sherwood number Comparison for Different Flow Fields

As shown in figure 7 the simulated results closely correlate with the analytical solution for potential flow. Because of this the influence of the Reynolds number beyond the change in Pe can not be depicted in any algorithm trained on the data. To estimate the error the boundaries in which the solution must lie namely the Sherwood numbers for creeping flow and the Sherwood numbers which are simulated with hydrodynamics, which closely resemble the potential flow solution are used. To do so the relative difference ΔSh between the reactive Sherwood numbers for both flow fields in comparison to the data with simulated hydrodynamics is introduced.

$$\Delta Sh = \frac{Sh_{hydro} - Sh_{cf}}{Sh_{hydro}} \tag{5.8}$$

Here Sh_{hydro} is the Sherwood number obtained with the simulated hydrodynamics and Sh_{cf} is the Sherwood number, obtained by using the Satapathy solution. In figure 10 ΔSh is plotted against Da for the decay reaction. As seen in the graph for both Peclet numbers the difference in mass transfer between the

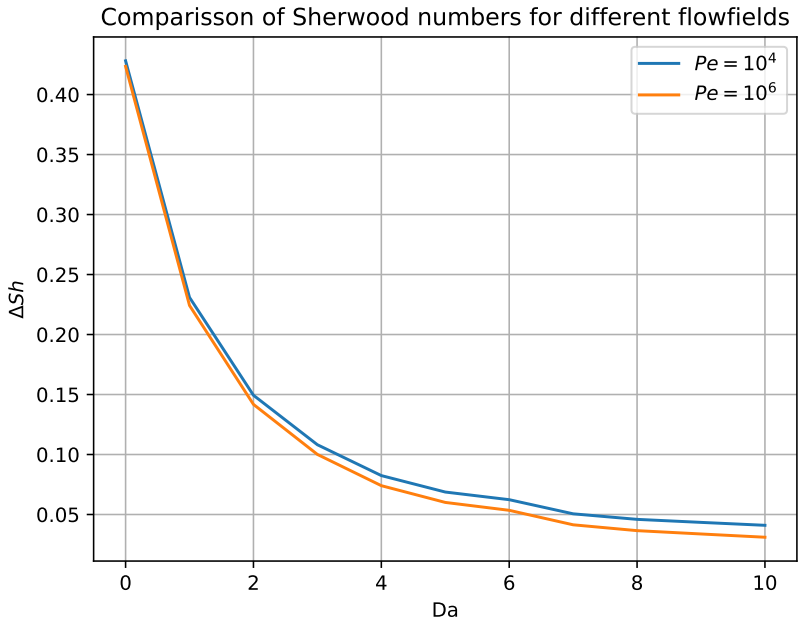

Figure 10: ΔSh against Da for different Peclet numbers.

creeping flow field and the one for potential flow converges towards 0 for large Damköhler numbers. While the dependency of Re on non reactive mass transfer can not be captured, this dependency is no longer important for higher Damköhler numbers. Thus for $Da > 7$ the error resulting from Re must be smaller than 5%. As the decay reaction is a special case of the single reaction the same results are expected for the single reactions if the system is reactive enough. What this means in particular is not clear so far.

5.4 Data Sets

For this thesis datasets for all four reactions were created. For the decay reaction a set of 1431 data points was created. The data points are spaced evenly in the feature space of the Peclet and Damköhler number. Note that the set also has changing Reynolds numbers, thus to use this set for algorithm training all Reynolds numbers except Re=40 should be purged, as Re has no influence on the Sherwood number. The Damköhler numbers range from 0 to 10 and the Peclet numbers range from 10^4 to 10^6. The single reaction has two datasets one with equally spaced data points with 2675 entries and a second set of 5400 data points, which consists of 3000 randomised points and a subset of the ordered set. The randomised points have a Reynolds number of 50 while the ordered ones have a Reynolds number of 40. The single Reaction data has the features Peclet number $Pe \in [10^4, 10^6]$, Damköhler number $Da \in [0, 10]$, diffusivity ratio D_B/D_A and concentration ratio between the bulk species concentration far from the interface, and the transfer species interface concentration c_B/c_A, both in $[0.1, 10]$. The parallel consecutive Reaction set contains 426 randomly spaced data points with the features Pe, Da_{AB}, Da_{AP}, D_B/D_A, D_P/D_A and c_B/c_A, all in the same ranges as presented for the single reaction for the specific feature type. The parallel competitive reaction dataset contains 3000 randomised data points with the features Pe, Da_{AB}, Da_{AC}, D_B/D_A, D_C/D_A, c_B/c_A and c_C/c_A, also all of these are in the same ranges as presented for the single reaction.
One simulation finished in a quarter to a full day depending on the reaction type on one cluster core. For similar problems such data sets can therefore be created in little time, if a multitude of cores are available.

5.5 Algorithm Comparison

To compare and access the capabilities of the different algorithms first their dependency on hyper parameters and prediction time is studied on the single and parallel competitive reaction data. The decay reaction only has two features, thus it would not generate much insight, also the consecutive reaction with its six features will behave very similar to the competitive reaction data, which is why only single and competitive reactions are analysed. With these results a grid search optimisation is used to tune the different algorithms on the different reaction types. Note, that the grid search uses cross validation, meaning, that the training set is further divided and trained, while always leaving one of the subsets ot of the training. The chosen hyper-parameters are those which score best on each left out subset test. The algorithms are trained and evaluated on the randomised data, except for the decay reaction as here no randomised data is available.

5.5.1 Polynom Regression

In figure 11 the dependency of the algorithms score and influence of the polynomial order on the latency is depicted. Both training and test score nearly overlap for all polynomials. A purely linear regression already reaches scores of 0.845 on the single reaction data. With an increasing polynomial order the score increases up to 0.97 for p=10. Usually polynoms of higher order tend to over-fit the data, but since the simulated data is not subject to noise over-fitting is unlikely. Note that this graph was made with $\alpha = 10$. Different values of α might lead to different scores but the trend will be the same. On the right side of figure 11 the corresponding prediction latency is plotted. It increases exponentially with the order of the polynom and reaches values of 50 seconds for p=10. In figure 12 the complexity and latency for the competitive

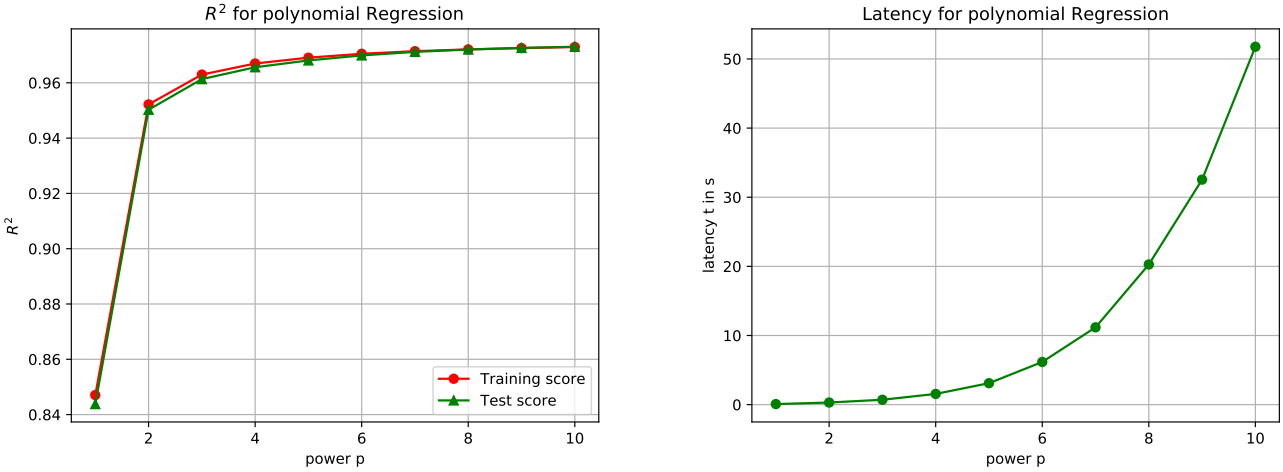

Figure 11: Complexity curve (left) and prediction latency (right, 10^6 predictions) for polynomial regression on the single reaction data ($\alpha = 10$).

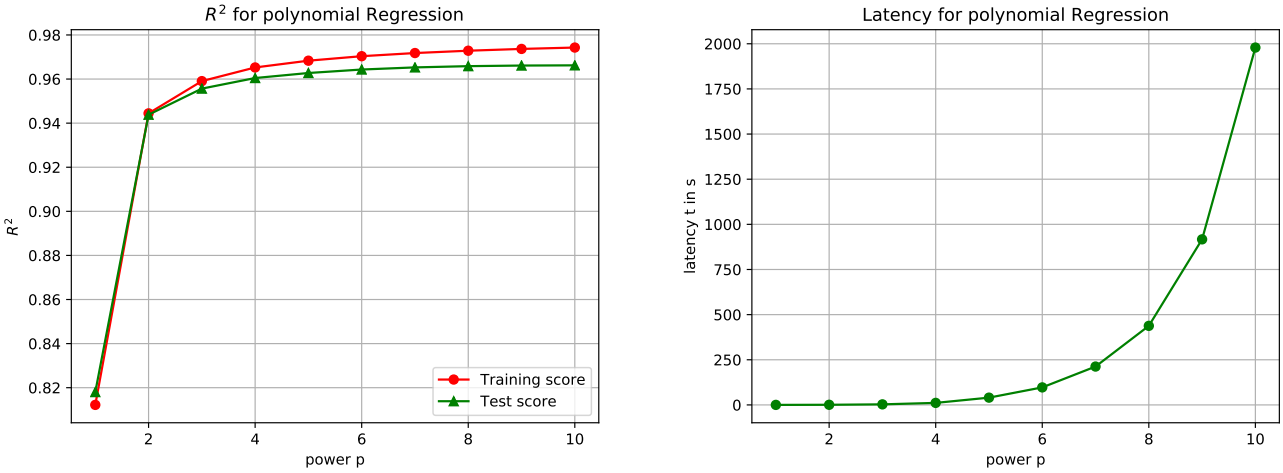

Figure 12: Complexity curve (left) and prediction latency (right, 10^6 predictions) for polynomial regression on the competitive reaction data ($\alpha = 10$).

reaction data is depicted. Overall the same trends are visible, but the training and test scores now diverge for p>2. The highest reached scores are 0.974 for training and 0.968 for test data. The latency also scales exponentially with the polynom power, but as it also scales quadratic with the number of features the polynom of power 10 now has a prediction latency of $1979s$. The improvement in score for higher polynom orders becomes smaller, but the required prediction time doubles. Because of the diminishing improvements, only polynoms of forth and second order are analysed, as higher polynoms are too expensive in terms of prediction latency.

In figure 13 the learning curves for these two polynoms are shown. In a learning curve the score on test and training data is plotted against the number of samples used for algorithm training. All curves, with the exception of the forth order polynom on the competitive reaction data, reach plateaus. This indicates, that

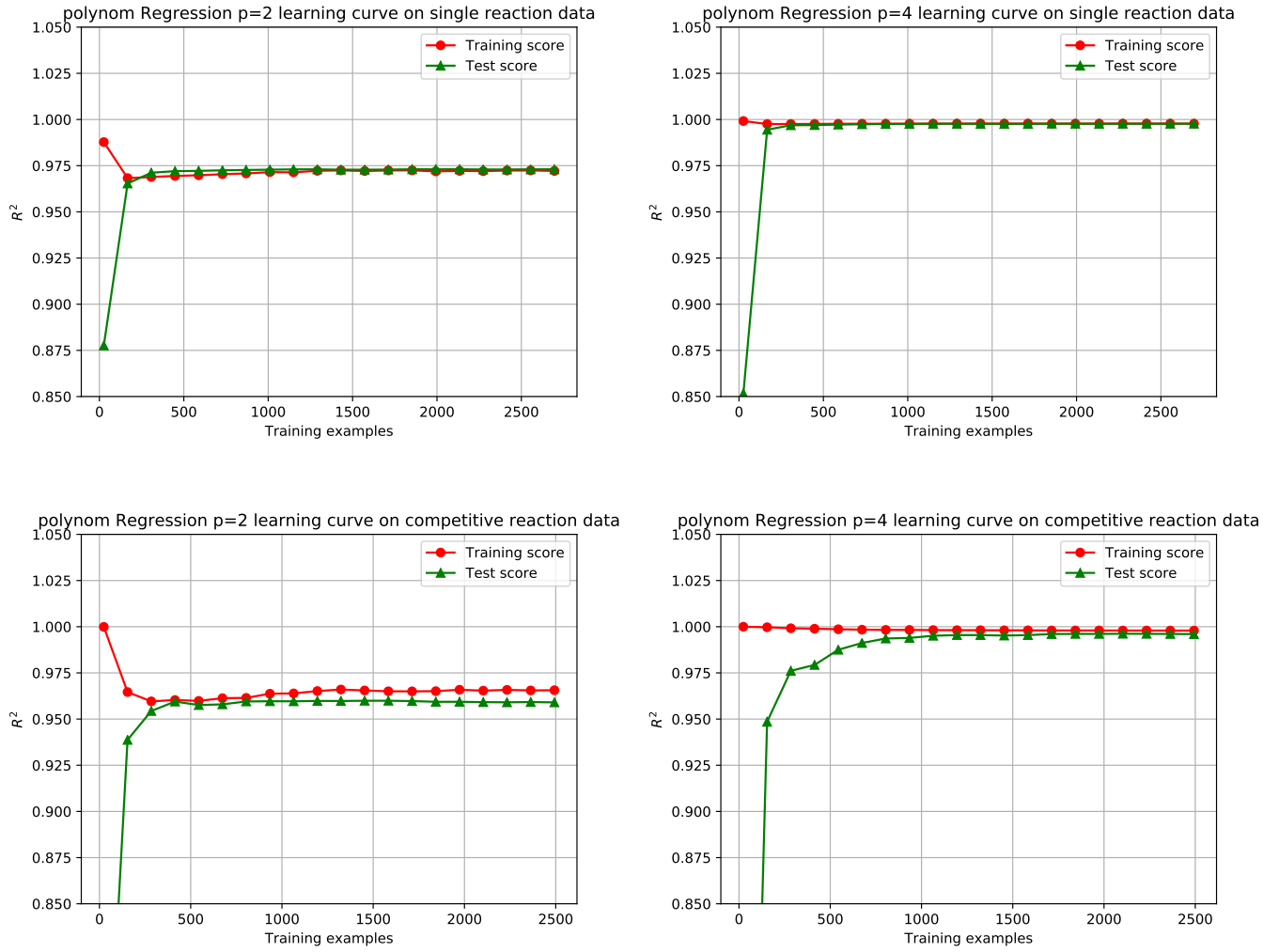

Figure 13: Learning curves for polynomial Regression, left for quadratic polynom, right polynom of forth order,single reaction in the upper row and competitive reaction in the lower row (hyper parameters from tables in 5.5.4).

both algorithms on both data sets reach sample independent solution as the score does no longer improve with more training samples. On the single reaction data both polynoms reach a plateau at 250 training samples. The polynom of second order reaches a plateau ar 400 training samples on the competitive reaction data. The polynom of forth order improves up to 2500 samples but reaches a near constant value at 1300 samples. The training score on the competitive reaction data for the quadratic polynom does not match the score of the test set. This indicates over-fitting, as if this would not be the case both lines should overlap. As both test and train score do have a limit for the quadratic polynom on the competitive reaction data the polynom can not fit the trends on the data, as they are of higher order. In the other three cases the test and training scores overlap, which indicated that no over-fitting occurs. For the case of less than 200 training points the score is significantly worse on all algorithm data set pairings, as here not enough data points are provided to capture the trends in the data. For experimental results over-fitting would be a more sever problem, as the data would be subject to random noise.

5.5.2 Kernel Based Algorithms

In figure 14 the complexity curves for KRR and SVR are plotted for both reaction types. The SVR depends on C which is the penalty parameter of the internally used error term. The KRR depends on α which is correlated to C for SVR as $\alpha = (2 \cdot C)^{-1}$ [Ped+17c]. The graphs for both reaction types are nearly

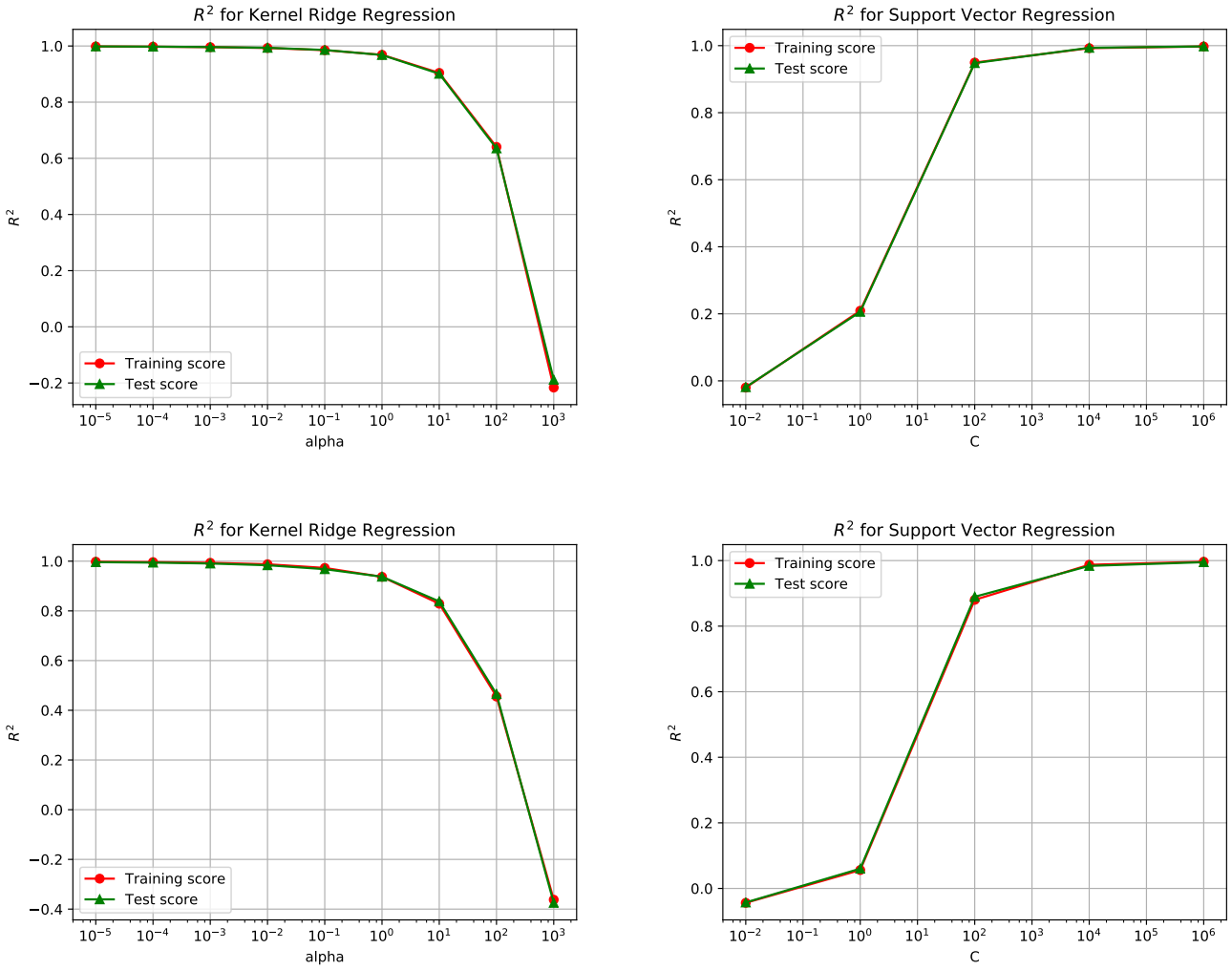

Figure 14: Complexity Curves for kernel based regression on the single reaction data (upper row) and competitive reaction data (second row), Kernel Ridge Regression on the left, Support Vector Regression on the right.

identical. Also test and training score are nearly identical for all graphs. For α values below 10^{-2} the score of the KRR tends to one. For larger values they are decreasing rapidly. For SVR C should be above 10^6, as here the score tends to one. For smaller values of C the score converges to zero. As α is similar to C^{-1} these results are to be expected. As for higher values of C the error becomes weighted higher, so overall results improve. However, this is here only possible as the data is not a noisy function. Such high values for C may lead to over-fitting if random noise is present in the data. As for polynomial regression learning curves are used to evaluate the sample requirements of these algorithms (in figure 15).

The kernel ridge regression reaches a training score of almost 1 at about 700 samples on the single reaction

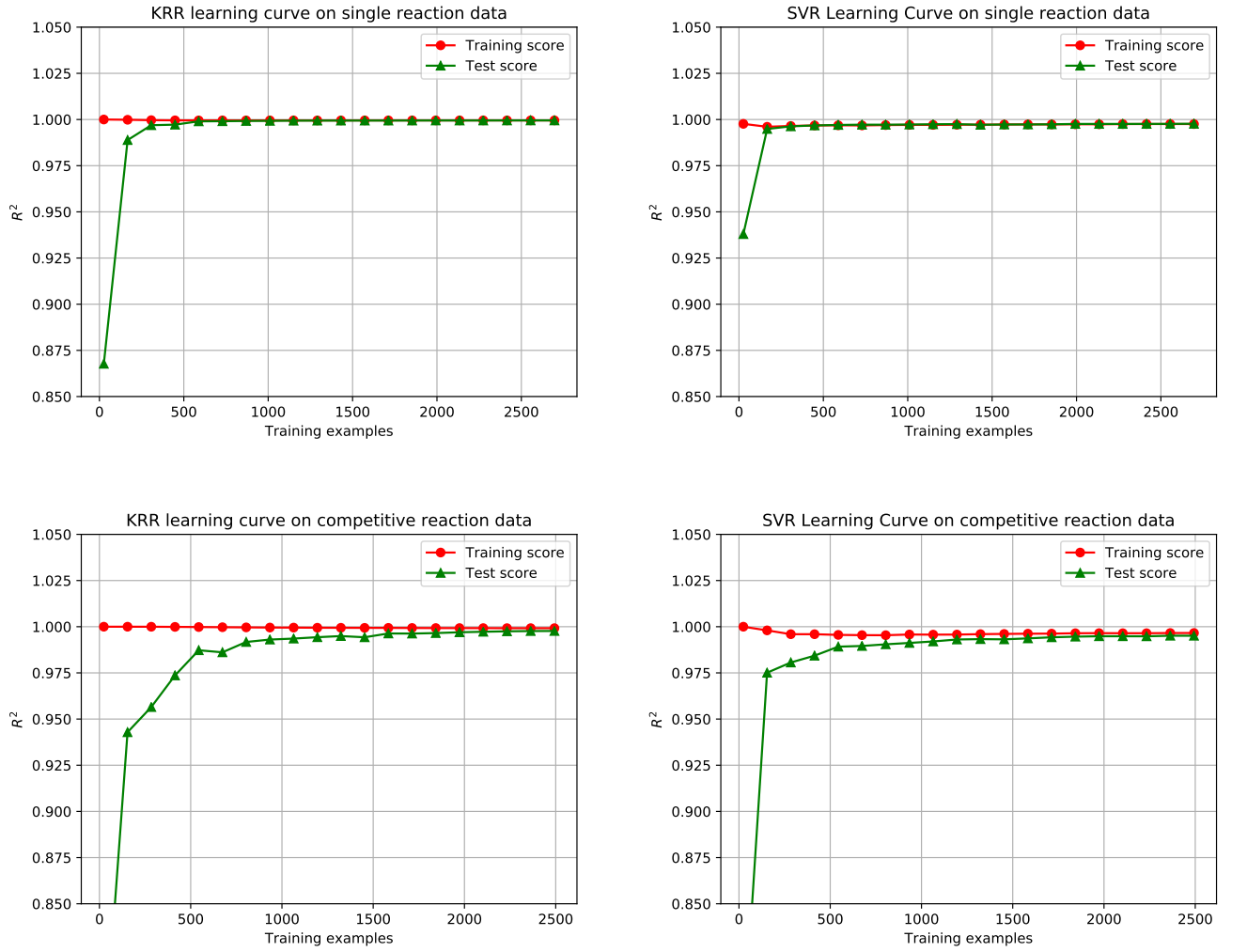

Figure 15: Learning Curves for SVR($C = 10^6$, right) and KRR ($\alpha = 10^{-7}$, left) on single reaction data (upper row) and competitive reaction data (lower row)

data. From there onwards the test and training scores are the same as expected. SVR reaches a slightly lower score but needs only 300 samples to do so. For SVR test and training score also overlap. On the competitive reaction data both test scores converge towards the training scores. The training scores for KRR are constant for both reaction types, while the training score for SVR decreases slightly for less than 200 samples in both reaction types. The score stays constant for more than 200 data points. As already mentioned SVRs and KRRs prediction times scale with the number of training samples provided. While this is not interesting for the competitive reaction as here the hole dataset is needed to reach the desired score, for the single reaction data the plateau is reached already at 700 samples, therefore no more than 700 samples should be used. This depenency is shown in figure 16, where the prediction latency for 10^5 predictions for a single reaction is plotted for both algorithms against the number of training samples. Both algorithms scale linearly with the training size, but SVR has a higher slope and takes longer for every test size. As shown in the graph the single and decay reaction algorithm should be trained on a smaller training set of only 700 samples as here the prediction latency is only 1/3 of the time needed on the

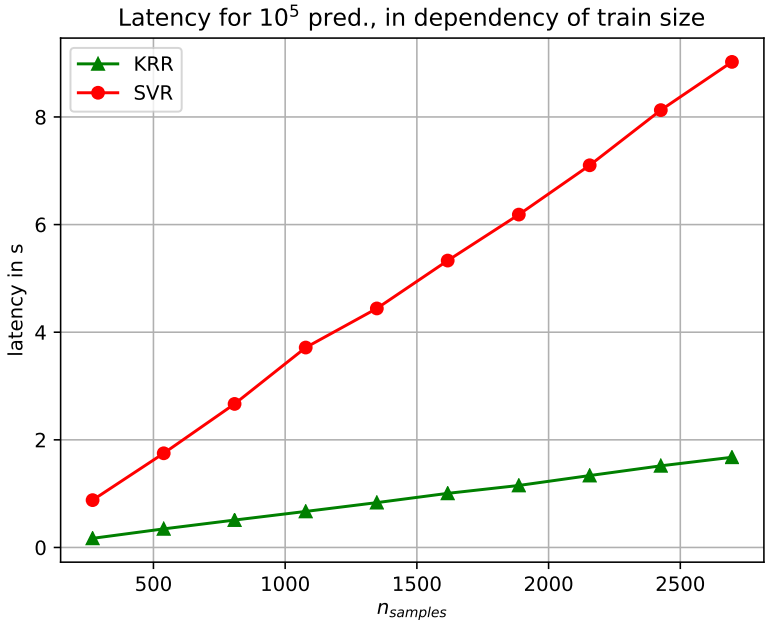

Figure 16: Prediction latency for 10^5 samples on single reaction data, for kernel based algorithms in dependency of training size (KRR: $\alpha = 10^{-7}$, SVR: C=1).

complete training set. In the following assessment SVR will no longer be tested, as it needs more training time, prediction time and yields similar results as KRR on all four data sets.

5.5.3 Decision Tree Regression

For the decision trees the main parameter tuned is the $min_{sampleSplit}$, which is the minimal number of samples necessary to build a new leaf. As this hyper-parameter directly controls the depth of the tree it has an influence on the prediction latency. In figure 17 the complexity curve and latency for 10^6 predictions are shown.

As expected the training-score is reduced with increasing $min_{sampleSplit}$, as for $min_{sampleSplit} = 2$ each data point becomes its own leaf. Note that the training-score in this case is perfect. On both the single and competitive reaction data the test-score is nearly constant up to $min_{sampleSplit} = 10$. For the single reaction data the score even slightly increases for $min_{sampleSplit} = 4$. This showcases that the $min_{sampleSplit}$ of two might score perfect on the training set but over-fits the data. Since our data is not subject to noise this effect is small, thus the over-fitting has no large impact on the score. As the latency decreases on both sets with increasing $min_{sampleSplit}$ it would be beneficial to set $min_{sampleSplit}$ to a higher value than two and lower than ten, as this would lead to unchanged scores but increased prediction speeds, but as the latency is only about 1/10 of a second this would only bring measurable performance gains for very large applications. It is also interesting that the latencies for both reactions are nearly identical. In contrast to the other algorithms the latency of the tree does not scale with the number of features but logarithmic with the size of the trainings-set. As both sets have roughly the same size the prediction latencies are also comparable. The overall score is at 0.969 on the single reaction data and 0.91 on the competitive reaction data. To further increase the R^2 score the random forest regression is tested. The complexity

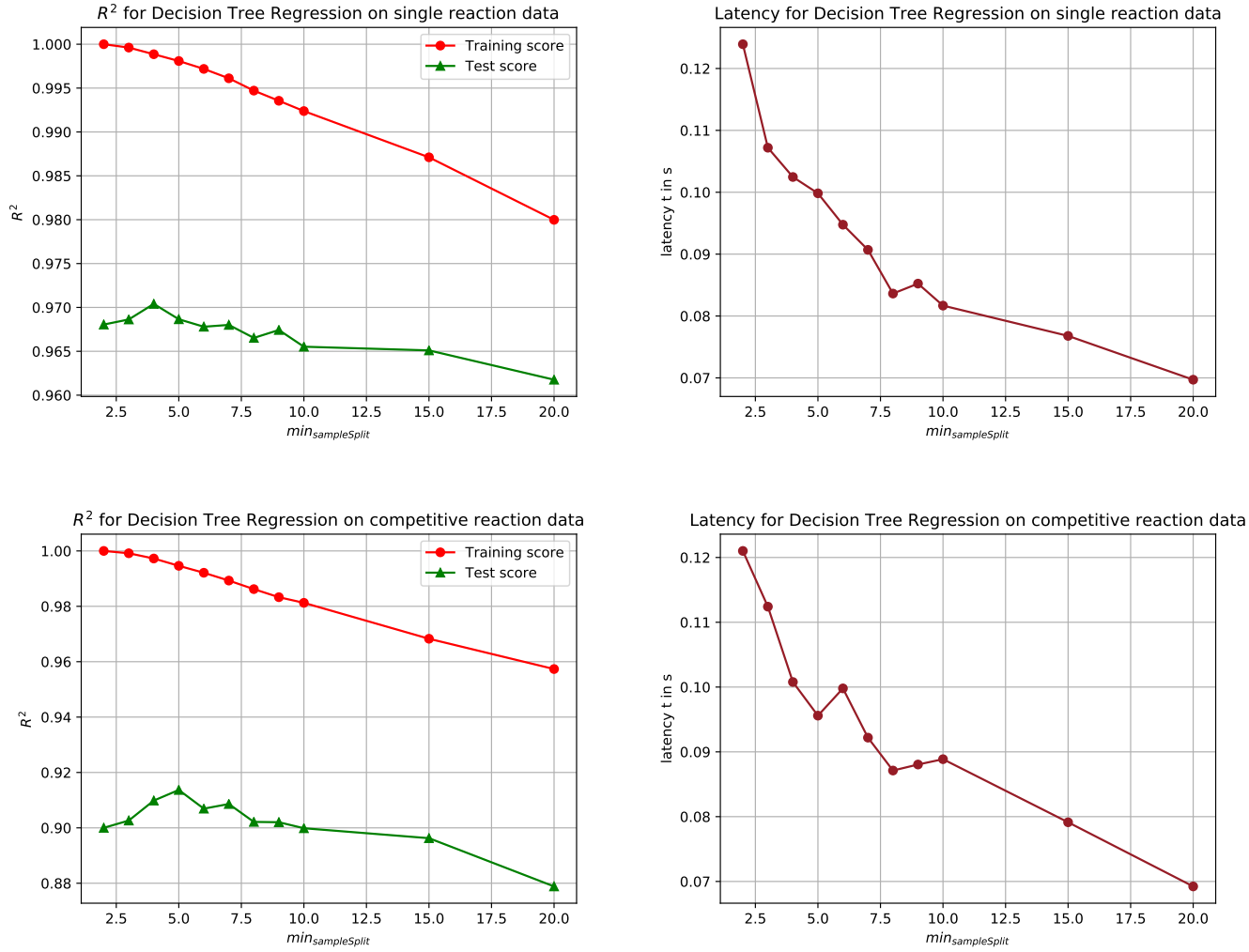

Figure 17: complexity curve and latency (10^6 predictions) for decision tree regression on the single reaction data (upper row) and parallel competitive data (lower row).

and latency curve for this algorithm in dependency of n_e, the number of estimators, is shown in figure 18. The number of estimators denotes the number of trees which are used to make the prediction. For both reactions the latency scales linearly with n_e. This was to be expected, as the forest is just a superposition of many trees. As already mentioned for the decision trees the latencies on both sets are nearly identical since it does not scale with the number of features. On the single reaction data the score on the test-set is now always below 1, but the test score is at about 0.982 for n_e above 128. Above this value of n_e the score does no longer increase. Thus the increase in n_e and the resulting longer latencies are unnecessary. For the competitive reaction data the result looks similar but only a score of 0.968 is achieved. Also 200 estimators are required to get to this value. At $n_e = 64$ a spike can be seen in the test score. It is most likely a result of the non deterministic nature of this approach. With further tuning it might be possible to get the required estimators to lower levels, but such attempts would be beyond the scope of this thesis. To evaluate how many training samples are needed the learning curves for both decision tree and random forest regression are plotted in figure 19. As seen in the upper left the test score on the single reaction data increases with more data, but reaches a plateau at 2200 samples and a R^2 score of 0.97. The training score

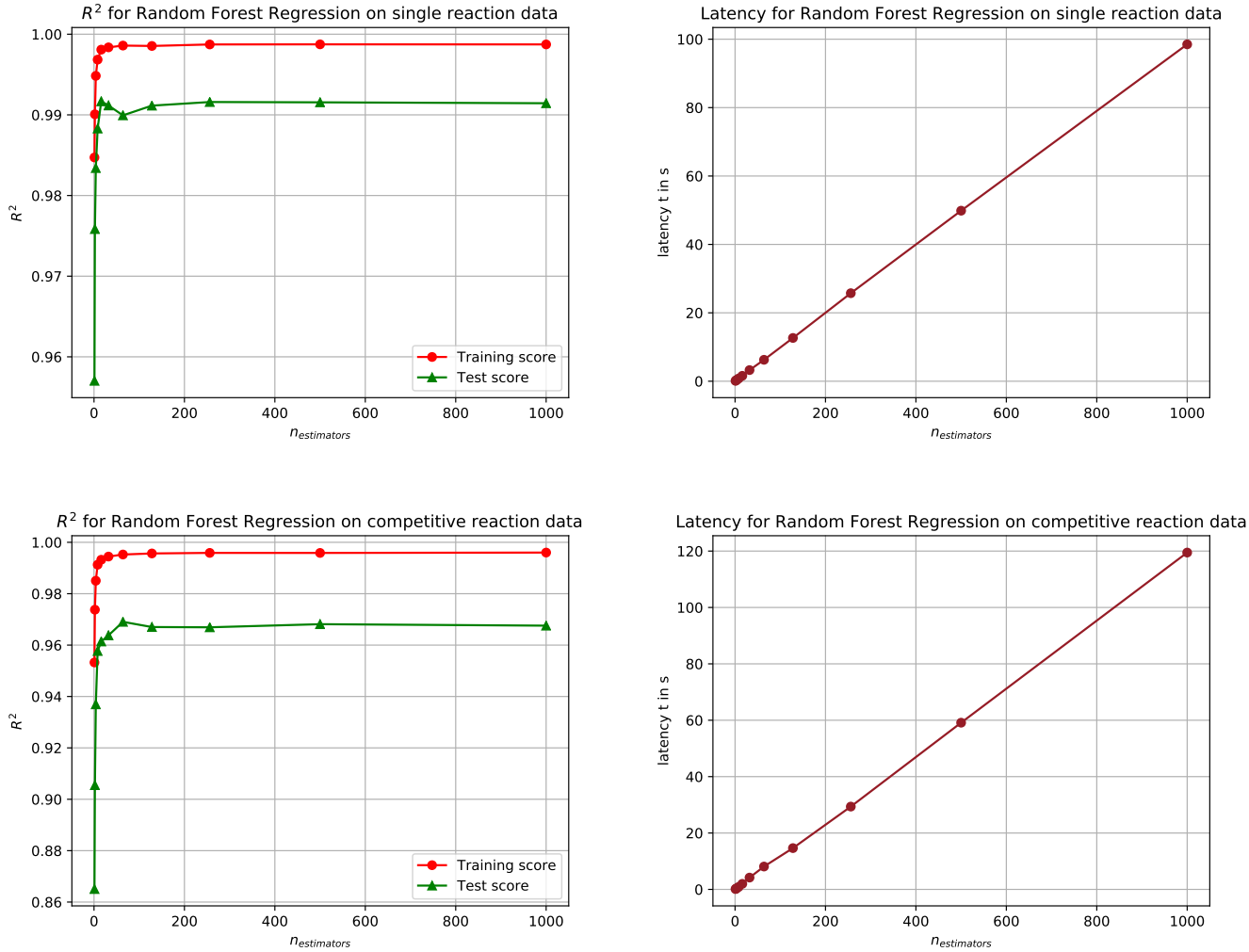

Figure 18: Complexity curve and latency (10^6 predictions) for random forest regression on the single reaction data (upper row)and parallel competitive data (lower row), $min_{sampleSplit} = 2$.

tends towards one but does not reach a plateau. The training results for the random forest regression on the single reaction data looks similar, but the test score is about 0.99. As here no real plateau is visible the score might increase further if more data is provided. The decision tree only reaches a test score of 0.9 on the full competitive reaction dataset. Note that the graph of the test score has many spikes and does not always increase with additional data. This is due to the high $min_{sampleSplit}$ and the instability of decision trees. Slightly different training sets may lead to different trees which do more poorly on the test set, despite the fact that more data is provided. Here more data is needed to further increase the score. The random forest regression does not show this instability, as the test score is mostly smooth and the training score is also smooth in contrast to the decision tree results on the left. The algorithm reaches scores of 0.97. As with the single reaction data the algorithm seems to have reached a plateau, but the plateau appears at 1750 samples. A further increase in samples might lead to a further increase in test score. Note that prediction latency also scales with the training set size for tree based algorithms. The influence of this is not shown here as the learning curves show no plateau which is reached early. Thus a decrease in training size would cost accuracy. As the tree search algorithms are fast and not accurate

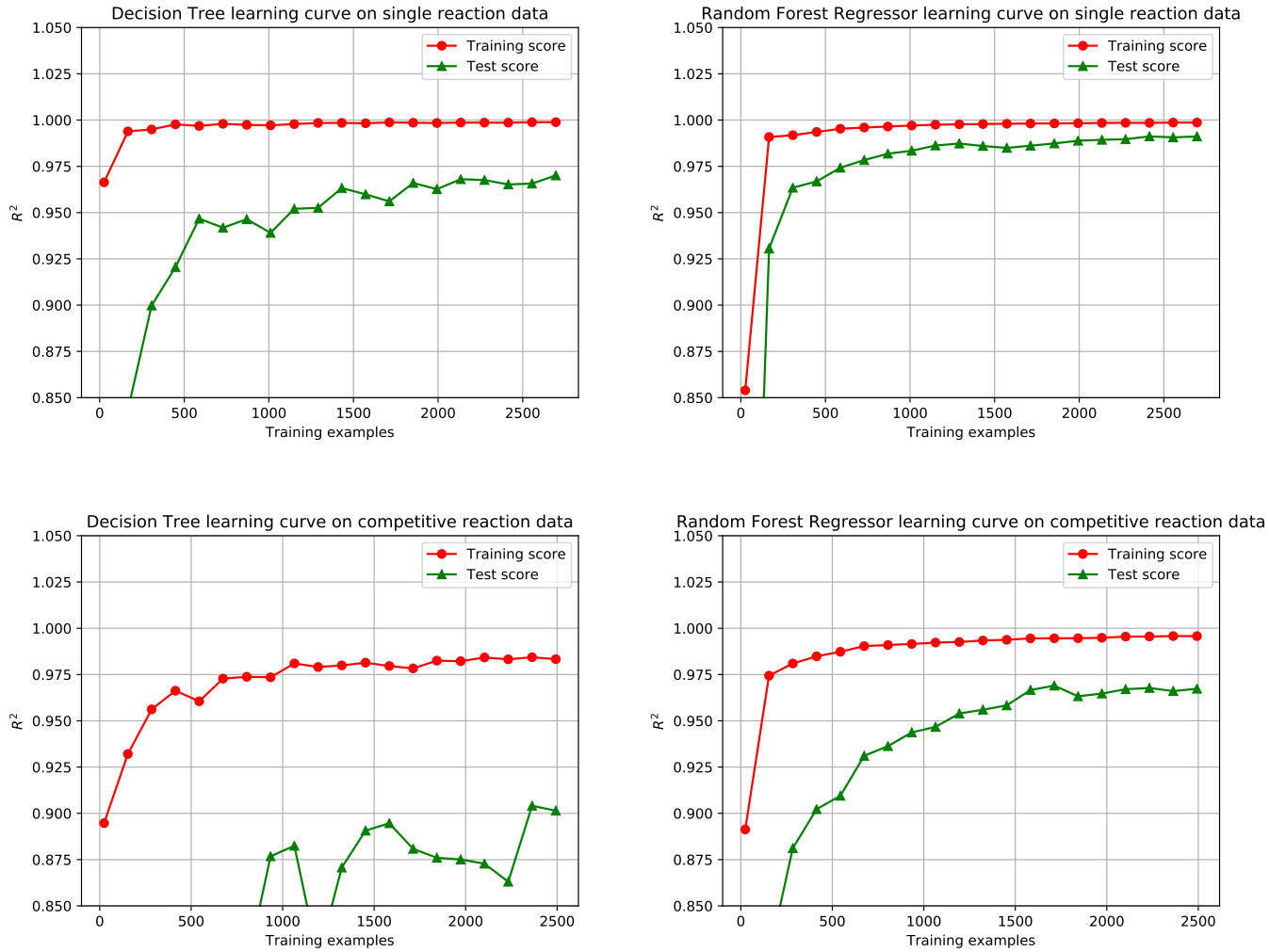

Figure 19: learning curves for decision Tree(left, $min_{sampleSplit} = 9$) and random forest regression (right, $n_e = 200$) on single (upper row) and competitive reaction data (lower row).

this should not be done. Furthermore, the influence of smaller training samples is similar to the scaling of the latency with the $min_{sampleSplit}$ hyper parameter, as the prediction time does only depend on the tree size. So if a speed-up is required it should be implemented by increasing the $min_{sampleSplit}$, since then all available information is used.

5.5.4 Algorithm Evaluation

The performance of the algorithms on the different datasets is presented in table 7 to 10. KRR ($n_s = 200$) denotes an kernel ridge algorithm which was trained on only 200 training points. This leads to faster prediction times. For the decay reaction no speed up is seen, since the trend is not so complex. Thus the larger algorithm does not use more support vectors and is equally fast. On the consecutive reaction data the partially trained kernel is slower due to the poly kernel used instead of the rbf kernel. Note that this was done by the gridsearch optimisation to improve the score. As this training set consists only of 400 samples at the time of training the result of both KRR algorithms are also expected to be closer together. The decision tree algorithm has the lowest prediction latency on all datasets, while the random forest is slowest

on the decay reaction data. The random forest is overall slower at predictions than polynom regression and faster than KRR, with the exception of the consecutive reaction data as this training set is small. Both tree based algorithms perform worse in R^2 than the other algorithms. Only on the competitive reaction data the random forest is slightly better than the polynom regression for p=2 (0.9665 to 0.9590), but has a latency ten times higher than the polynom. The polynom regression of forth order and the fully trained Kernel Ridge regression offer the highest score on all datasets. However, the polynom regression offers faster prediction times, as it is 44 times faster than KRR on the single reaction data. For the competitive reaction the ratio is only 5.9, as the polynom latency scales quadratically with the dimension of the feature space. For all four reaction types polynom regression of forth order offers the highest score and has the lowest prediction latency. Therefore, on these four datasets the polynom regression should be used. If very few data points are provided KRR performs similar, but an increase in training data increases the latency for KRR. Thus fine tuning is needed to yield best results. Polynomial regression on the other hand does not scale with training size, and also needs few training data to yield good results. Polynom regression becomes very slow if the feature space becomes to large or the underlying data has trends of higher order. To construct models for such systems a combination of decision tree and quadratic polynom regression might be beneficial, where a decision tree divides the feature space into subspaces which than can be fitted with a simple polynom or even just a linear function. This might be a possibility to use the high score of the polynomial regression without the weak scaling characteristics.

Algorithm	Hyperparameters	R^2 on test set	latency for 10^6 predictions
Decision Tree	min samples split: 2	0.9798	0.0571s
Random Forest	min samples split: 2, n_e: 200	0.9959	5.1013s
Kernel Ridge Regression	alpha: 1e-08, kernel: rbf	0.9999	3.2094s
KRR($n_s = 200$)	alpha: 1e-08, kernel: rbf	0.9999	3.2116s
Polynomial Regression p=2	alpha: 4, solver: auto	0.9852	0.0833s
Polynomial Regression p=4	alpha: 0.3, solver: auto	0.9996	0.3473s

Table 7: Performance of algorithms on decay Reaction dataset.

Algorithm	Hyperparameters	R^2 on test set	latency for 10^6 predictions
Decision Tree	min samples split: 3	0.9377	0.1025s
Random Forest	min samples split: 3, n_e: 200	0.9808	18.4686s
Kernel Ridge Regression	alpha: 1e-07, kernel: rbf	0.9979	88.1555s
KRR($n_s = 200$)	alpha: 0.0001, kernel:rbf	0.995	6.4796s
Polynomial Regression p=2	alpha: 0.001, solver: auto	0.9591	0.3937s
Polynomial Regression p=4	alpha: 6, solver: auto	0.9968	2.211s

Table 8: Performance of algorithms on single Reaction dataset.

Algorithm	Hyperparameters	R^2 on test set	latency for 10^6 predictions
Decision Tree	min samples split: 4	0.6217	0.0711s
Random Forest	min samples split: 3, n_e: 200	0.9384	3.0335s
Kernel Ridge Regression	alpha: 1e-05, kernel: rbf	0.9923	12.7469s
KRR($n_s = 200$)	alpha: 0.0001, kernel: poly	0.9858	16.4101s
Polynomial Regression p=2	alpha: 6, solver: auto	0.9603	0.7587s
Polynomial Regression p=4	alpha: 10, solver: auto	0.9868	7.8892s

Table 9: Performance of algorithms on parallel consecutive Reaction dataset.

Algorithm	Hyperparameters	R^2 on test set	latency for 10^6 predictions
Decision Tree	min samples split: 9	0.9015	0.0951s
Random Forest	min samples split: 2, n_e: 200	0.9665	10.0104s
Kernel Ridge Regression	alpha: 1e-07, kernel: rbf	0.9977	84.9183s
KRR($n_s = 200$)	alpha: 0.0001, kernel: rbf	0.9752	6.7639s
Polynomial Regression p=2	alpha: 10, solver: svd	0.9590	1.08s
Polynomial Regression p=4	alpha: 10, solver: auto	0.9960	14.2682s

Table 10: Performance of algorithms on parallel competitive Reaction dataset.

5.6 Volume Change Simulation

Using the previously implemented algorithms to predict Sh the volume change of bubbles can be simulated as a simple 1D model. The following system is modelled according to the model for mass transfer derived in [Kas+15]. The change of the amount of substance N_i in the bubble can be expressed by

$$\frac{\partial N_i}{t} = -\beta A_\Sigma (c_{i,\Sigma} - c_{i,\infty}) \quad . \tag{5.9}$$

Using the definition of the Sherwood number (2.28) and $A_\Sigma = \pi d_b^2$ the equation becomes

$$\frac{\partial N_i}{t} = (c_{i,\infty} - c_{i,\Sigma}) \pi D_i Sh_i d_b \quad . \tag{5.10}$$

The concentration of species i in the bulk $c_{i,\infty}$ is equal to zero for the first simulation. The interface concentration of species i $c_{i,\Sigma}$ can be expressed using Henry's law

$$c_{i,\Sigma} = \frac{(c_{bulk} + c_{i\Sigma}) p X_i}{H_i} \approx \frac{c_{bulk} p X}{H_i} \tag{5.11}$$

where c_{bulk} is the total concentration of the bulk phase, meaning the concentration of H_2O molecules in water, p the pressure, H_i the Henry coefficient for the species and X_i the molar fraction of species i in the bubble.

$$X_i = \frac{N_i}{\sum_k N_k} \tag{5.12}$$

As initially only CO_2 is inside the bubble, $X_{CO_2} = 1$. Note that in the equation $c_{i,\Sigma}$ is neglected as it is three orders of magnitude smaller than c_{bulk}. As the bubble rises in the continuous phase the pressure varies since

$$p = p_{ambient} + g * \rho_{bulk} * h \tag{5.13}$$

$$\frac{\partial h}{\partial t} = U \quad , \tag{5.14}$$

where h is the current depth of the bubble and U the rise velocity. If assumed that U is always at a steady state the velocity can be calculated from the drag force.

$$F_D = 0.5 \rho_{bulk} C_D A U^2 = g \Delta\rho \frac{\pi}{6} d_b^3 = F_b \tag{5.15}$$

$$U = \sqrt{\frac{4 \Delta\rho \, g \, d_b}{3 \rho_{bulk} C_D}} \tag{5.16}$$

Here F_D is the drag force, F_b the buoyancy force, A the front surface , $\Delta\rho$ the difference in density between bulk and dispersed phase and C_D the drag coefficient which can be modelled for different Reynolds numbers according to table 5.2 in [CG78, p. 112]. For the simulation correlation B, C and D are used depending on the Reynolds number.

$$C_D = \frac{24}{Re}(1 + 0.1315 Re^{0.82 - 0.05 \cdot log_{10}(Re)}), \qquad 0.01 < Re \leq 20 \tag{5.17}$$

$$C_D = \frac{24}{Re}(1 + 0.1315 Re^{0.6305}), \qquad 20 < Re \leq 260 \tag{5.18}$$

$$C_D = 10^{1.6435 - 1.1242 \cdot log_{10}(Re) + 0.1558 \cdot (log_{10}(Re))^2}, \qquad 260 < Re \leq 1500 \tag{5.19}$$

The density difference $\Delta\rho$ can be calculated according to

$$R_{Sp} = \frac{\sum_i N_i \cdot M_i}{\sum_i N_i} \tag{5.20}$$

$$\Delta\rho^j = \rho_{bulk} - (p^j / (R_S p * T)) \quad . \tag{5.21}$$

Here R_{Sp} is the specific gas constant of the mixture inside the bubble. Assuming Re is known the Sherwood number can be predicted with one of the machine learning algorithms as $Pe_i = Re \, \nu / D_i$. As last unknown variable the bubble diameter can be evaluated

$$d_b = 2 \sqrt[3]{\frac{3}{4\pi} \frac{\sum_i N_i}{c_{bubble}}} \quad , \tag{5.22}$$

where N_i is the amount of substance in the bubble which is modelled by equation (5.9) and c_{bubble} the total concentration of the dispersed phase which depends on the pressure as shown by the ideal gas equation

$$c_{bubble} = \frac{p}{RT} \quad . \tag{5.23}$$

Here R is the universal gas constant and T the temperature. The pressure inside the bubble is higher than outside. This is modeled by the Young-Laplace equation, but as this increase in pressure is small compared to the surrounding pressure it is neglected. With these equations an Euler forward method can be implemented to calculate the Volume change over time. By solving

$$Re^j = \frac{U^{j-1} d_b^{j-1}}{\nu} \tag{5.24}$$

$$C_D^j = \frac{24}{Re}(1 + 0.1315(Re^j)^{0.6305}) \tag{5.25}$$

$$p^j = p_{ambient} + \rho_{bulk} g h^{j-1} \tag{5.26}$$

$$\Delta\rho^j = \rho_{bulk} - (p^j/(R_{Sp} * T)) \tag{5.27}$$

$$U^j = \sqrt{\frac{4\Delta\rho^j g d_b^j}{3\rho_{bulk} C_D}} \tag{5.28}$$

$$h^j = h^{j-1} - U^{j-1}\Delta t \tag{5.29}$$

$$c_{i\Sigma}^j = \frac{p^j c_{bulk}}{H} \tag{5.30}$$

$$N_i^j = N_i^{j-1}(c_{i,\infty} - c_{i\Sigma}^j)\pi D_i Sh_i^j d_b^{j-1}\Delta t \tag{5.31}$$

$$c_{bubble}^j = \frac{p^j}{RT} \tag{5.32}$$

$$d_b^j = 2\sqrt[3]{\frac{3}{4\pi}\frac{\sum_i N_i^j}{c_{bubble}^j}} \tag{5.33}$$

$$V^j = \frac{4}{3}\pi(\frac{d_b^j}{2})^3 \quad . \tag{5.34}$$

Where Sh_i^j was predicted with the Peclet number $Pe = Re^j Sc$ and the decay reaction polynom regression model of forth order. As the Damköhler number is set to 0 this algorithm predicts physical mass transfer. In [Mer+17] the volume change of CO_2 bubbles rising in degassed water is analysed. In table 11 the parameters used in the study and needed constants are depicted. With the previously introduced euler forward solver the same system can be simulated. In figure 20 the results from simulation and experiment are compared.

Parameter	Value
liquid	H_2O
gas	CO_2
h_0	$2m$
ρ_{bulk}	$997.04\,kg/m^3$
c_{bulk}	$55.4 \cdot 10^3 mol/m^3$
H	$1660 \cdot 10^5 mol/(m^3 Pa)$
D_A	$1.92 \cdot 10^{-9} m^2/s$
R	$8.3144598 kg\,m^2/(s^2 mol K)$
T	$298.15K$
R_{CO_2}	$188.9 J/(kg\,K)$
g	$9.81 m/s^2$
ν	$1 \cdot 10^{-6} m^2/s$
Δt	$0.0001s$

Table 11: Parameters of the experiment in [Mer+17].

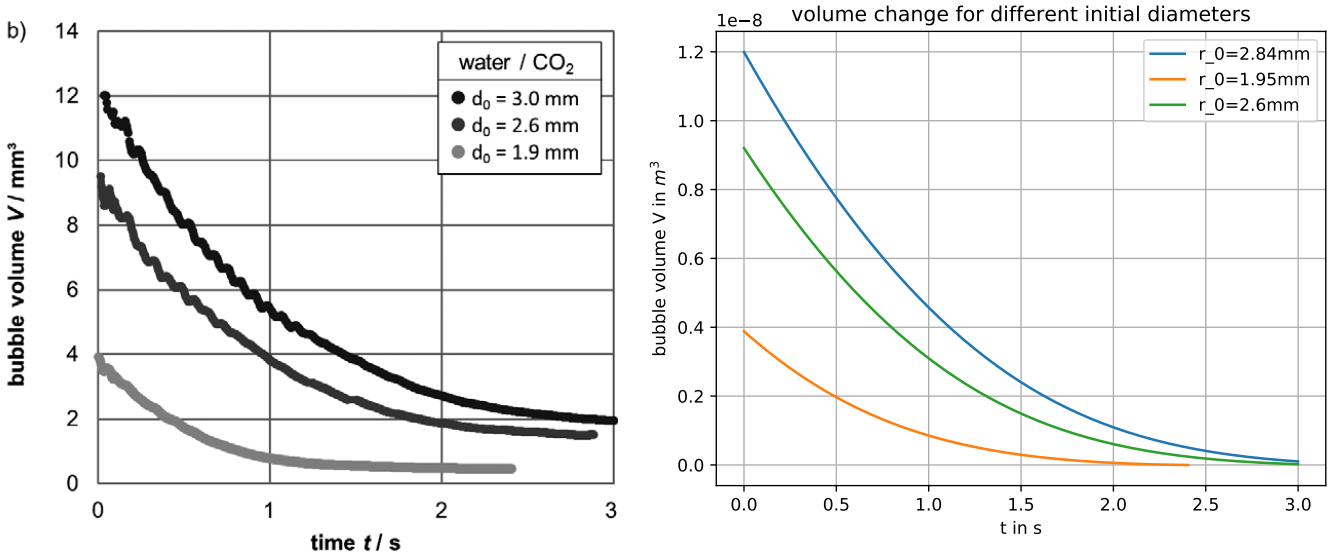

Figure 20: Comparisson of simulation with CO_2 only (right) and experiment (left graph taken from [Mer+17]).

Between $0s$ and $0.5s$ simulation and experiment agree very well with each other, but afterwards the simulated bubble converges towards a volume of zero, while the experiments show lasting bubble volume. This might be the result of another species transferring from the bulk into the bubble. As the same algorithm can be used to predict mass transfer from the bulk into the bubble the species N_2 and O_2 are introduced, to test if their presence can explain the lasting volume. In table 12 the additional values assumed for the simulations are depicted. The bulk concentrations of the different species are calculated by Henry's law and the assumption that the concentration in water is in an equilibrium state with the concentration of the species in the air, hence the pressure is $10^5 Pa$ and the molar fractions of the species X_{CO_2}, X_{O_2} and X_{N_2} being 0.05, 0.21 and 0.7805 for these calculations, accordingly. Note that the other gases found in the atmosphere are neglected because of their low concentrations and high Henry numbers. The results of this setup are compared to the experiment in figure 21. Both graphs still show similar

Parameter	Value
liquid	H_2O
gas	CO_2
h_0	$2m$
ρ_{bulk}	$997.04 kg/m^3$
c_{bulk}	$55.4 \cdot 10^3 mol/m^3$
H_{CO_2}	$1.660 \cdot 10^8 Pa$
H_{O_2}	$4.4 \cdot 10^9 Pa$
H_{N_2}	$9.1 \cdot 10^9 Pa$
D_{CO_2}	$1.92 \cdot 10^{-9} m^2/s$
D_{O_2}	$2.1 \cdot 10^{-9} m^2/s$
D_{N_2}	$1.88 \cdot 10^{-9} m^2/s$
$c_{CO_2,bulk}$	$1.6685 mol/m^3$
$c_{O_2,bulk}$	$0.2646 mol/m^3$
$c_{N_2,bulk}$	$0.475 mol/m^3$
$p_{ambient}$	$1 bar$
R	$8.3144598 kgm^2/s^2 molK$
T	$298.15K$
g	$9.81 m/s^2$
ν	$1 \cdot 10^{-6} m^2/s$

Table 12: Parameters for the simulation of conjugated mass transfer after experiment in [Mer+17].

volumes in the first $0.5s$ as here the influence of the other species is still small. But the simulation now also shows non diminishing bubble volume, but it is still much smaller than the results from the experiments. In figure 22 the concentrations of the three species inside the bubble are presented for one bubble. The concentration of CO_2 falls rapidly as expected, but the other two species grow too slow to explain the lasting volume in the experiment. As the experiment in [Mer+17] was carried out under a not further specified inert atmosphere it is tested if an argon atmosphere and water in equilibrium with this atmosphere would explain the terminal volume. In table 13 the values for argon are presented and in figure 23 the results are shown.

The resulting terminal volumes are now closer to the experiment but the volume is still only 50% of the experimental value. The graphs still agree between 0 and 0.5s. In figure 24 the concentrations inside the bubble are plotted. Because Argon reaches higher concentrations than the other two species the

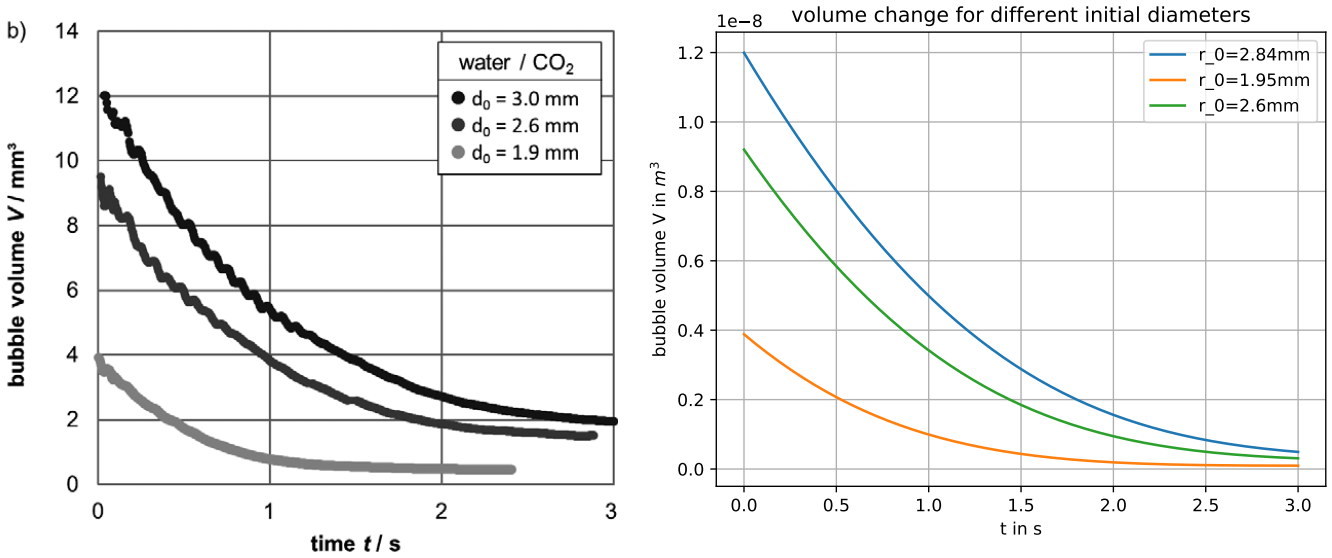

Figure 21: Comparisson of simulation with conjugated mass transfer(right) and experiment (left graph taken from [Mer+17])

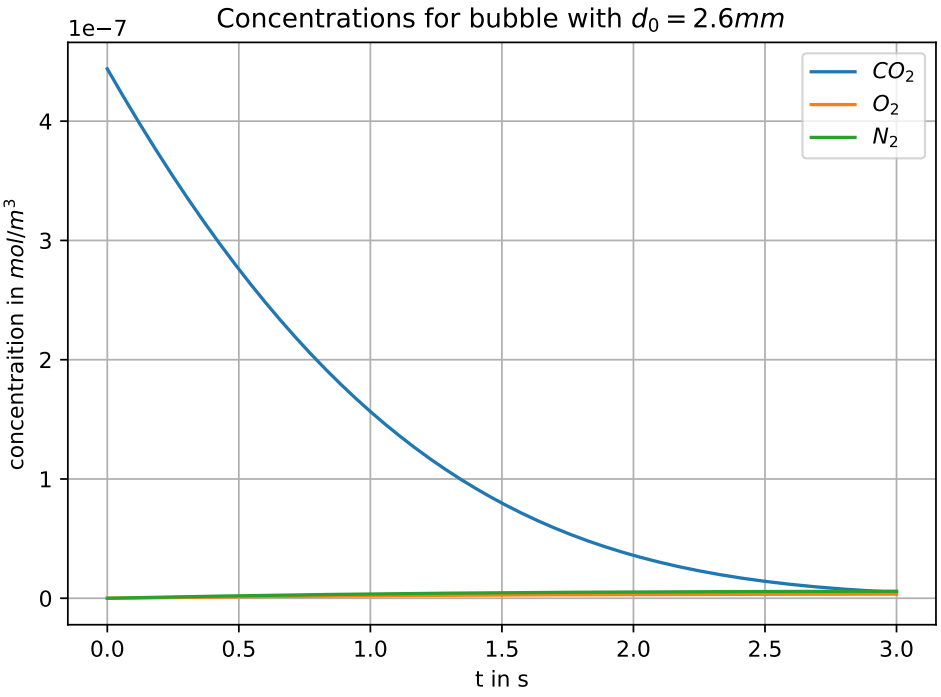

Figure 22: Species concentration inside the bubble for the conjugated mass transfer simulation.

Parameter	Value
H_{Ar}	$4.1 \cdot 10^9 Pa$
D_{Ar}	$2 \cdot 10^{-9} m^2/s$
$c_{Ar,bulk}$	$1.35 mol/m^3$
M_{Ar}	$39.948 \cdot 10^{-3} kg/mol$

Table 13: Parameters for Argon in the simulation of conjugated mass transfer (values taken from wikipedia).

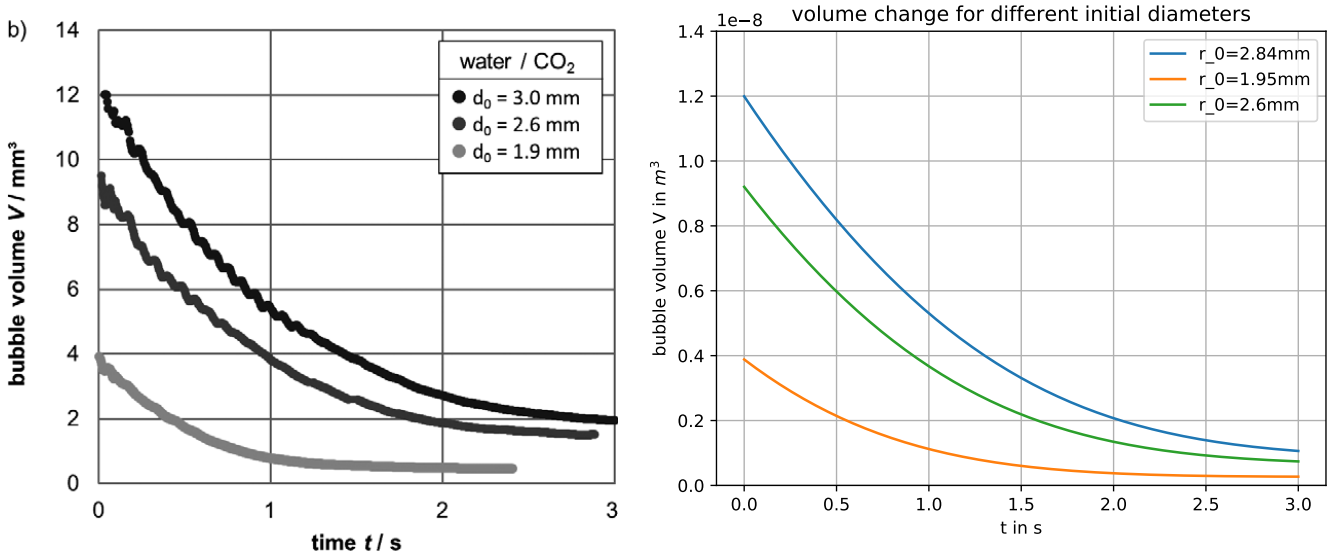

Figure 23: Comparisson of simulation in Argon atmosphere with experiment (left graph taken from [Mer+17])

terminal bubble volume increases. The difference is due to the many simplifications used. First the model to predict mass transfer rates was trained for spherical bubbles. In reality the bubble is no longer spherical. Also steady state is assumed for the bubble velocity. Also the bubble rises vertically in the simulation. In reality bubbles take curved paths and spiral upwards. This leads to different velocity profiles and thus Peclet numbers, which are used for the prediction. Also the real gas concentrations inside the water are unknown and were only assumed.

5.6.1 Error Evaluation

Even tough the simulated terminal volume is only 50% of the experimental results the simulation can be used to estimate the difference between the system with just one species and the case of conjugated mass transfer. To access this error the previously studied system is used and for the transfer species the values of CO_2 are assumed, but the transfer species now reacts in an decay reaction inside the bulk. The system is simulated for just the transfer species and afterwards the simulation is carried out with Argon diffusing into the bubble. The relative deviation $\Delta V = (V_{conjugated} - V_{ideal})/V_{conjugated}$ is plotted over time for different bubble radii in figure 25. Different Henry coefficients and reaction rate constants are shown. The relative difference ΔV converges to one for all cases, as the the ideal volume where only a species leaves the bubble approaches zero. Close to t=0s the difference is small, thus it would be possible to calculate the mass transfer rates with little error even if conjugated transfer is neglected. For larger initial diameters

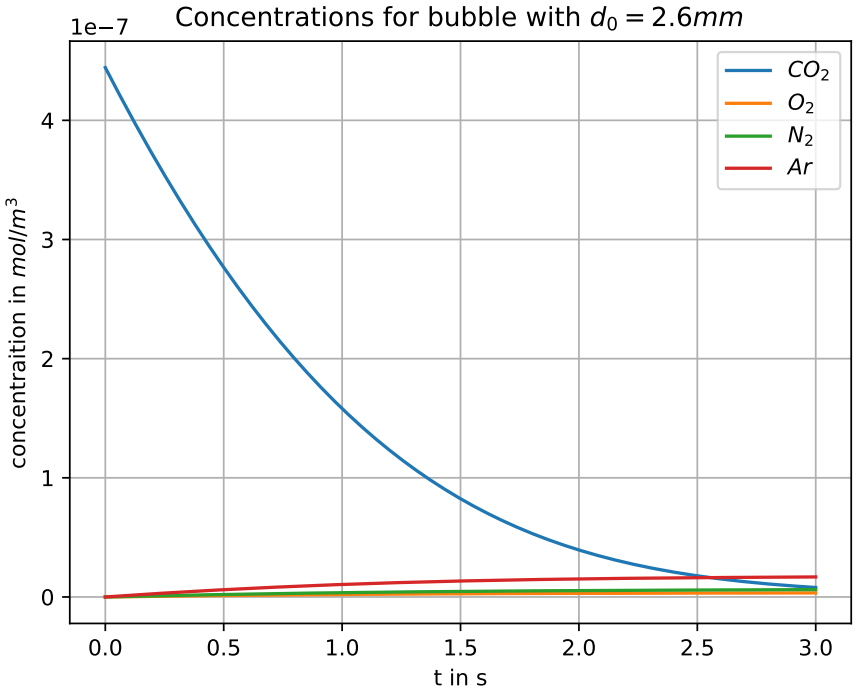

Figure 24: Species concentration inside the bubble under Argon atmosphere.

the error is small for a longer period of time. With higher reaction rate constants the deviation converges faster towards 0. With higher Henry coefficients the deviation curve becomes less steep. The influence of the Henry coefficient of the transfer species is larger than the influence of the reaction rate constant. Below 0.5s the difference between both models is below 10% for all cases shown, except bubbles with initial diameters of 1mm. This agrees well with the previous findings, where experiment and simulation agreed well for t<0.5s.

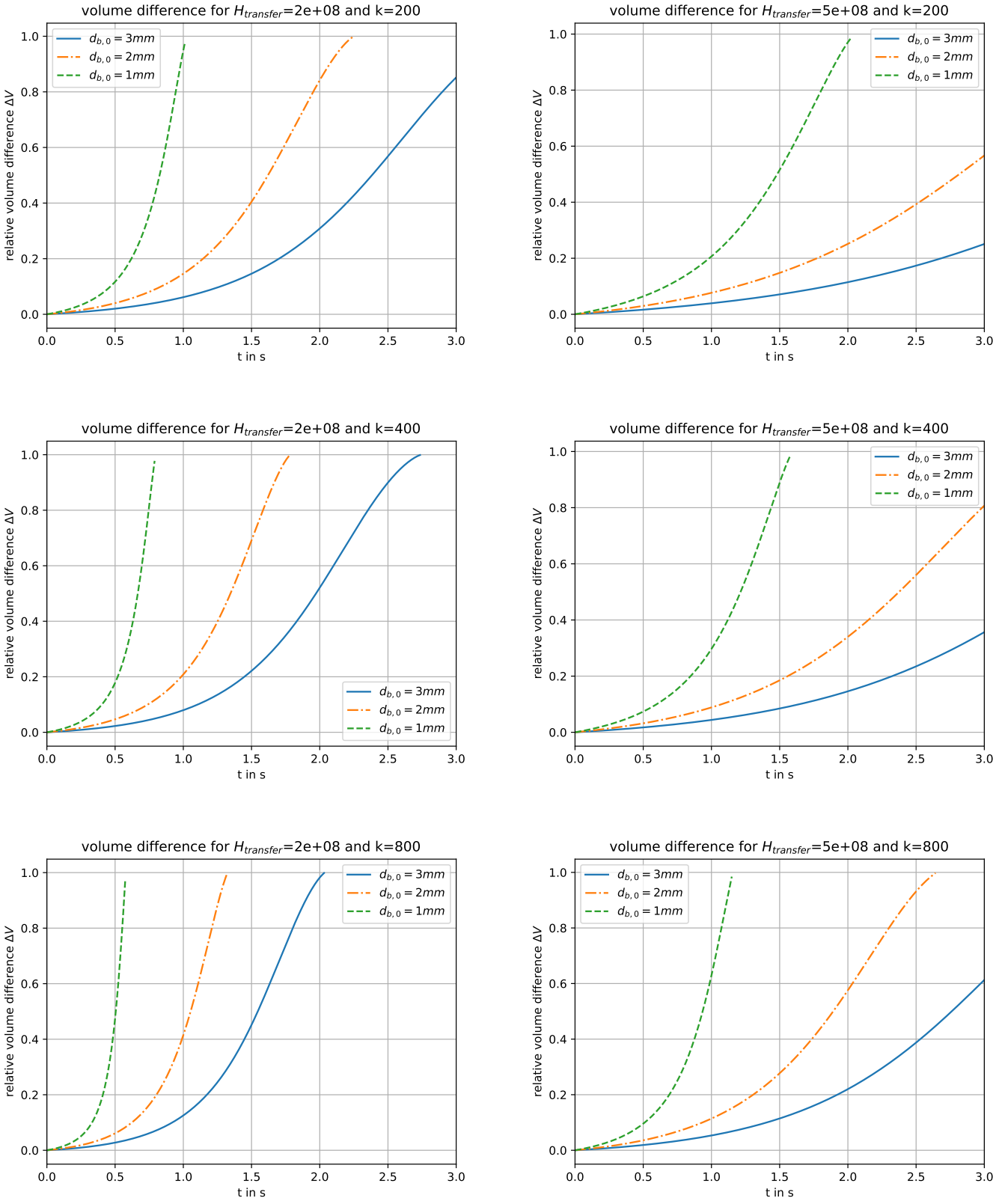

Figure 25: Comparisson of volume change for decay reaction with and without conjugated mass transfer of Argon, for different Henry coefficients of the transfer species and reaction rate constants ($d_{b,0} = 3mm$, transfer species paramters are identical to the ones of CO_2).

6 Conclusion and Outlook

The solution of hydrodynamics and reaction kinetics around a bubble are in terms of computational effort hard to analyse. Thus a 2D fixed bubble model with radial symmetric flow was used to conduct a parameter study on four prototypical reactions. The internal mass transfer resistance was neglected and the concentration inside the bubble was assumed to be constant in space and time. The simulations either used a simulated velocity field which closely resembles potential flow solutions or the flow fields were modeled according to the Satapathy and Smith solution for creeping flows [SS60].
Comparing the results to correlations for non-reactive mass transfer the simulations with the Satapathy solution agree very well with the correlations for creeping flow conditions. The simulated hydrodynamics do not capture the influence of the Reynold number as depicted by the correlations of Takemura and Lochiel. Instead they closely resembles the results for potential flow fields, since the assumption of a slip condition on the bubble interface simplifies the problem.
Three known models for the enhancement factor for single reactions namely film theory, renewal model and penetration theory are compared to the simulations. All three result in nearly the same prediction, however, penetration and film theory are implicit and expensive to compute. All correlations predict higher mass transfer rates in comparison to the simulations.
As already stated the simulations closely resemble the potential flow solution and thus are assumed to overpredict the mass transfer. But it was found, that, for high Damköhler numbers the resulting Sherwood numbers for potential flow fields and creeping flow fields converge towards the same value. Thus for decay reactions for $Da > 7$ the difference between both Sherwood numbers is below 5%, compared to 45% for solely physical mass transfer. This means that for highly reactive systems the data predicts the Sherwood number accurately, as the real solution must lie between the boundaries of potential and creeping flow.
Afterwards machine learning regression models are trained on the datasets. It is shown that kernel ridge regression and polynomial regression are most suited to predict the Sherwood numbers on these datasets. Both reach R^2 scores of 0.99 on all datasets. Polynomial regression is however capable of faster predictions on these small feature spaces.
With the polynomial model the volume change of a CO_2 bubble rising in a water column is simulated. First only mass transfer from the bubble into the bulk is considered. Afterwards the same simulation is carried out with the transfer from the bulk phase into the bubble as the species N_2 and O_2 are also considered. The results are compared to the experiment carried out in [Mer+17]. While the initial mass transfer rates and volumes are in good agreement, the experiment shows a terminal bubble volume much larger than what is observed in the simulation.

As shown with the simulation of volume change the surrogate models implemented can be used in scale reduced methods. In a next step these algorithms could be used to implement Euler-Euler or Euler-Lagrange simulations. However, to use such models to there full potential the feature space needs to be widened. As this study only analysed spherical bubbles at low Reynolds numbers a large variety of factors such as the influence of eccentricity, wake structures for higher Reynolds numbers, surfactants and the influences of oscillations were not analyzed, not to mention effects encountered in bubble swarms. To use such regression models on the full bubble feature space it is necessary to build three things. First as the feature space is vast, it is necessary to find a way to build a good model on as little data as possible. Thus instead

of simulating randomly and then train a model on the data, data generation and model training should happen simultaneously. The model could be used to predict where additional data would generate the most performance increase. Second the dimension of the input features must be reduced if the full feature space should be used, as otherwise the prediction time would be to long. Thus method to combine features are needed. Lastly it is necessary to combine correlations or models automatically. Otherwise it would be necessary to train the model every time additional data is introduced.

A Appendix

A.1 Bisection algorithm for E-factor Calculation

```
def film(Ha,E_i,E):
    E_max=E_i*0.95
    E_min=E*0.8
    eta=lambda E_iter:sqrt((E_i-E_iter)/(E_i-1))
    E_iter=lambda eta:Ha*eta/tanh(Ha*eta)
    f_mid=10
    i=0
    while  abs(f_mid)>0.01 and i<10000:
        f_max=E_iter(eta(E_max))-E_max
        f_min=E_iter(eta(E_min))-E_min
        E_mid=(E_max+E_min)/2
        f_mid=E_iter(eta(E_mid))-E_mid
        print(i,E_max,E_mid,E_min)
        if (f_max*f_mid)< 0:
            E_min=E_mid
        else:
            E_max=E_mid
        i+=1
    return E_mid
def penetration(Ha,E_i,E):
    E_max=E_i*0.95
    E_min=E*0.8
    f_mid=10
    E_mid=0
    i=0
    eta=lambda E_iter:sqrt((E_i-E_iter)/(E_i-1))
    E_iter=lambda eta:(Ha*eta+pi/(8*Ha*eta))*erf(2*Ha*eta/sqrt(pi))+0.5*exp(-4*4*Ha**2*eta**2/pi)
    while abs(f_mid)>0.01 and i<10000:
        f_max=E_iter(eta(E_max))-E_max
        f_min=E_iter(eta(E_min))-E_min
        E_mid=(E_max+E_min)/2
        f_mid=E_iter(eta(E_mid))-E_mid
        if (f_max*f_mid)<0:
            E_min=E_mid
        else:
            E_max=E_mid
        i+=1
    return E_mid
```

Figure 26: code to calculate the enhancment for film and penetration theory

Bibliography

[Bel14] J. Bell. "Working with Decision Trees". In: *Machine Learning*. John Wiley & Sons, Inc, 2014, pp. 45–68. ISBN: 9781119183464. DOI: 10.1002/9781119183464.ch3.

[Bre01] L. Breiman. "Random Forests". In: *Machine Learning* 45.1 (Oct. 2001), pp. 5–32. ISSN: 1573-0565. DOI: 10.1023/A:1010933404324.

[Bun17] Statistisches Bundesamt. *Unternehmen, Beschäftigte, Umsatz und Investitionen im Verarbeitenden Gewerbe und Bergbau: Deutschland, Jahre, Wirtschaftszweige*. Aug. 29, 2017. URL: https://www-genesis.destatis.de/genesis/online;jsessionid=B296CD35EEB3847FDECADE44F3880EF5.tomcat_GO_2_3?operation=previous&levelindex=2&levelid=1503991937502&step=2.

[CP17] H. Chakdar and S. Pabbi. "Chapter 9 - Algal Pigments for Human Health and Cosmeceuticals". In: *Algal Green Chemistry*. Ed. by Rajesh Prasad Rastogi, Datta Madamwar, and Ashok Pandey. Amsterdam: Elsevier, 2017, pp. 171–188. ISBN: 978-0-444-63784-0. DOI: https://doi.org/10.1016/B978-0-444-63784-0.00009-6.

[CG78] R. Clift and J. R. Grace. *Bubbles, Drops and Particles*. 1.Edition. New York, London: Academic Press, 1978.

[Dan70] P.V. Danckwert. *Gas Liquid Reactios*. New York: McGraw-Hill Book Company, 1970.

[Dis74] W. J. Discoursey. "Absorbtion with chemical Reaction:Development of a new relation for the Danckwerts Model". In: *Chemical Engineering Science* 29 (1974), pp. 1867–1872.

[Fle14] S. Fleckenstein. "Modeling and direct numerical simulation of mass transfer from rising gas bubbles". Zugl.: Darmstadt, Techn. Univ., Diss. 2014. PhD thesis. Aachen: TU Darmstadt, 2014. ISBN: 978-3-8440-2909-3.

[GFB16] D. Grünling, S. Fleckenstein, and D. Bothe. "A subgrid-scale model for reactive concentration boundary layer for 3D mass transfer simulation with deformable fluid interfaces". In: *International Journal of Heat and Mass Transfer* 101 (2016), pp. 476–487.

[HMD91] Z. He, C. Maldarelli, and Z. Dagan. "The size of stagnant caps of bulk soluble surfactant on the interfaces of translating fluid droplets". In: *Journal of Colloid and Interface Science* 146.2 (1991), pp. 442–451. ISSN: 0021-9797. DOI: http://dx.doi.org/10.1016/0021-9797(91)90209-Q.

[HA64] H. Hikita and S. Asai. "Gas absorption with (m,n)th order irreversible chemical reaction". In: *Int.Chem.Eng.* 4.2 (1964), pp. 332–340.

[HT11] C. J. Hulatt and D. N. Thomas. "Productivity, carbon dioxide uptake and net energy return of microalgal bubble column photobioreactors". In: *Bioresource Technology* 102.10 (2011), pp. 5775–5787. ISSN: 0960-8524. DOI: http://dx.doi.org/10.1016/j.biortech.2011.02.025.

[Jun12] G. Juncu. "Unsteady-state mass transfer accompanied by a first-order chemical reaction from a binary gas bubble with changing volume". In: *International Journal of Heat and Mass Transfer* 55.15 (2012), pp. 4269–4275. ISSN: 0017-9310. DOI: http://dx.doi.org/10.1016/j.ijheatmasstransfer.2012.03.069.

[Jun11] G. Juncu. "Unsteady-state mass transfer from a binary gas bubble with changing volume". In: *International Journal of Heat and Mass Transfer* 54.1 (2011), pp. 669–677. ISSN: 0017-9310. DOI: http://dx.doi.org/10.1016/j.ijheatmasstransfer.2010.09.003.

[Jun02] Gh. Juncu. "The influence of the Henry number on the conjugate mass transfer from a sphere: II – mass transfer accompanied by a first-order chemical reaction". In: *Heat and Mass Transfer* 38.6 (June 2002), pp. 523–534. DOI: 10.1007/s002310100256.

[Kas+15] S. Kastens et al. “Mass Transfer from Single Taylor Bubbles in Minichannels”. In: *Chemical Engineering and Technology* 38.11 (2015), pp. 1925–1932. ISSN: 1521-4125. DOI: 10.1002/ceat.201500065.

[Khi05] J. G. Khinast. “Mikrovermischung in reaktiven deformierbaren Blasen- und Tropfenschwärmen”. In: *Chemie Ingenieur Technik* 77.11 (2005), pp. 1723–1736. ISSN: 1522-2640. DOI: 10.1002/cite.200500136.

[KKL03] J. G. Khinast, A. A. Koynov, and T. M. Leib. “Reactive mass transfer at gas–liquid interfaces: impact of micro-scale fluid dynamics on yield and selectivity of liquid-phase cyclohexane oxidation”. In: *Chemical Engineering Science* 58.17 (2003), pp. 3961–3971. ISSN: 0009-2509. DOI: http://dx.doi.org/10.1016/S0009-2509(03)00311-7.

[KR17] M. Krauß and Rzehak R. “Reactive absorption of CO 2 in NaOH: Detailed study of enhancement factor models”. In: *Chemical Engineering Science* 166 (2017), pp. 193–209.

[LC64] A.C. Lochiel and P. H. Calderbank. “Mass transfer in the continuous phase around axisymmetric bodies of revolution”. In: *Chemical Engineering Science* 19 (1964), pp. 471–484.

[Ltd17] The OpenFOAM Foundation Ltd. *OpenFoamFoundation*. June 19, 2017. URL: https://openfoam.org/.

[Mar+11] M. Martín et al. “Shape oscillating bubbles: hydrodynamics and mass transfer - a review”. In: *Bubble Science, Engineering & Technology* 3.2 (2011), pp. 48–63. DOI: 10.1179/1758897911Y.0000000006.

[Mer+17] D. Merker et al. “Mass Transfer in Reactive Bubbly Flows A Single-Bubble Study”. In: *Chemical Engineering and Technology* 40.8 (2017), pp. 1391–1399. ISSN: 1521-4125. DOI: 10.1002/ceat.201600715.

[NHB16] W.J. Nock, S. Heaven, and C.J. Banks. “Mass transfer and gas–liquid interface properties of single CO2 bubbles rising in tap water”. In: *Chemical Engineering Science* 140 (2016), pp. 171–178. ISSN: 0009-2509. DOI: http://dx.doi.org/10.1016/j.ces.2015.10.001.

[OSB73] L. Oellrich, H. Schmidt-Traub, and H. Brauer. “Theoretische Berechnung des Stofftransports in der Umgebung einer Einzelblase”. In: *Chemical Engineering Science* 28.3 (1973), pp. 711–721. ISSN: 0009-2509. DOI: http://dx.doi.org/10.1016/0009-2509(77)80005-5.

[Ped+17a] F. Pedregosa et al. *scikit-learn*. July 11, 2017. URL: http://scikit-learn.org/stable/index.html.

[Ped+17b] F. Pedregosa et al. *scikit-learn Decision Trees*. Sept. 14, 2017. URL: http://scikit-learn.org/stable/modules/tree.html.

[Ped+17c] F. Pedregosa et al. *scikit-learn linear Model*. Sept. 14, 2017. URL: http://scikit-learn.org/stable/modules/generated/sklearn.kernel_ridge.KernelRidge.html#sklearn.kernel_ridge.KernelRidge.

[Ped+11] F. Pedregosa et al. “Scikit-learn: Machine Learning in Python”. In: *Journal of Machine Learning Research* 12 (2011), pp. 2825–2830.

[Ras15] S. Raschka. *Python Machine Learning*. Birmingham: Packt Publishing Ltd., 2015. ISBN: 978-1-78355-513-0.

[SS60] R. Satapathy and W. Smith. “The motion of single immiscible drops through a liquid”. In: *Jornal of Fluid Mechanics* 10.4 (Oct. 1960), pp. 561–570.

[SBH] K. Siebertz, D. v. Bebber, and T. Hochkirchen. *Statistische Versuchsplanung*. Undetermined. VDI-Buch. ISBN: 978-3-642-05492-1. DOI: 10.1007/978-3-642-05493-8.

[TY98] F. Takemura and A. Yabe. “Gas dissolution process of spherical rising gas bubbles”. In: *Chemical Engineering Science* 53 (1998), pp. 2691–2699.

[VH48] P.D. Van Krevelen and P.J. Hoftijzer. “Kinetics of gas-liquid reactions Part I”. In: *Recueil des Travaux Chimiques des Pays-Bas* 67 (7 1948), pp. 563–586.

Bachelor-Thesis Statement

Thesis Statement pursuant to §22 paragraph 7 of APB TU Darmstadt

I herewith formally declare that I have written the submitted thesis independently. I did not use any outside support except for the quoted literature and other sources mentioned in the paper. I clearly marked and separately listed all of the literature and all of the other sources which I employed when producing this academic work, either literally or in content. This thesis has not been handed in or published before in the same or similar form. In the submitted thesis the written copies and the electronic version are identical in content.

Darmstadt, 19.09.2017

(Tim Jeremy Patrick Karpowski)